Article

Evidence of striped electronic phases in a structurally modulated superlattice

https://doi.org/10.1038/s41586-024-07589-5

Received: 4 January 2023

Accepted: 21 May 2024

Published online: 3 July 2024

Check for updates

A. Devarakonda[1,8], A. Chen[2], S. Fang[1], D. Graf[3], M. Kriener[4], A. J. Akey[5], D. C. Bell[5,6], T. Suzuki[7] & J. G. Checkelsky[1]✉

The electronic properties of crystals can be manipulated by superimposing spatially periodic electric, magnetic or structural modulations. Long-wavelength modulations incommensurate with the atomic lattice are particularly interesting[1], exemplified by recent advances in two-dimensional (2D) moiré materials[2,3]. Bulk van der Waals (vdW) superlattices[4–8] hosting 2D interfaces between minimally disordered layers represent scalable bulk analogues of artificial vdW heterostructures and present a complementary venue to explore incommensurately modulated 2D states. Here we report the bulk vdW superlattice $SrTa_2S_5$ realizing an incommensurate one-dimensional (1D) structural modulation of 2D transition metal dichalcogenide (TMD) *H*-TaS_2 layers. High-quality electronic transport in the *H*-TaS_2 layers, evidenced by quantum oscillations, is made anisotropic by the modulation and exhibits commensurability oscillations paralleling lithographically modulated 2D systems[9–11]. We also find unconventional, clean-limit superconductivity in $SrTa_2S_5$ with a pronounced suppression of interlayer relative to intralayer coherence. The in-plane magnetic field dependence of interlayer critical current, together with electron diffraction from the structural modulation, suggests superconductivity[12–14] in $SrTa_2S_5$ is spatially modulated and mismatched between adjacent TMD layers. With phenomenology suggestive of pair-density wave superconductivity[15–17], $SrTa_2S_5$ may present a pathway for microscopic evaluation of this unconventional order[18–21]. More broadly, $SrTa_2S_5$ establishes bulk vdW superlattices as versatile platforms to address long-standing predictions surrounding modulated electronic phases in the form of nanoscale vdW devices[12,13] to macroscopic crystals[22,23].

Incommensuration in crystals arises from the coexistence of two or more mutually incompatible periodicities[24]. Incommensuration can appear in forms spanning magnetic modulations in rare earth metals[25,26], in the arrangement of ions and molecules in graphite intercalation compounds[27] and as incommensurate charge-density waves (CDWs) in metallic systems[28]. Another prominent class is structurally incommensurate materials in which incommensuration appears as a spatial modulation of the crystal lattice. These materials, with mismatched periodicities of the lattice and modulation, are beyond the usual description of crystals and motivated the formulation of superspace group methods to describe their structures[29]. If the incommensurate modulation is weak and has a longer wavelength compared with the lattice periodicity, it can act as a perturbation to the underlying crystal[30], presenting a means to manipulate its electronic behaviour and design phases beyond those found in conventional crystals.

Semiconductor superlattices[30] are early examples of engineered incommensuration in which one-dimensional (1D) periodic modulations along the growth direction (Fig. 1a) are created by varying the chemical composition, for example, periodic aluminium (Al) doping into gallium arsenide (GaAs). Incommensuration is achieved by engineering the modulation wavelength λ such that λ/a is irrational (where a is the crystal lattice spacing). Lithographically patterned semiconductor heterostructures are another example (Fig. 1b) with incommensurate modulations superimposed on high-quality 2D electron gases (2DEGs). More recently, moiré patterns at lattice mismatched or rotationally faulted vdW heterointerfaces (Fig. 1c) have emerged as hosts for incommensurately modulated phases. Together, materials with engineered incommensuration have realized various intriguing electronic phenomena: semiconductor superlattices feature electronic mini-bands with non-linear electronic and optical properties[30,31], patterned 2DEGs exhibit new commensurability resonances[9–11] and moiré-patterned vdW heterostructures host an array of emergent correlated and topological phases[3,32,33]. A notable aspect of these existing platforms is their exceptionally low atomic-scale disorder, supporting high-mobility transport and fragile electronic ground states. Thermodynamically stable, incommensurately modulated bulk materials with comparable quality are desirable as readily accessible, complementary platforms to study modulated electronic states. Apart from fragile

[1]Department of Physics, Massachusetts Institute of Technology, Cambridge, MA, USA. [2] Department of Electrical Engineering and Computer Science, Massachusetts Institute of Technology, Cambridge, MA, USA. [3]National High Magnetic Field Laboratory, Tallahassee, FL, USA. [4]RIKEN Center for Emergent Matter Science (CEMS), Wako, Japan. [5]Center for Nanoscale Systems, Harvard University, Cambridge, MA, USA. [6]John A. Paulson School of Engineering and Applied Sciences, Harvard University, Cambridge, MA, USA. [7]Department of Physics, Toho University, Funabashi, Japan. [8]Present address: Department of Applied Physics and Applied Mathematics, Columbia University, New York, NY, USA. ✉e-mail: checkelsky@mit.edu

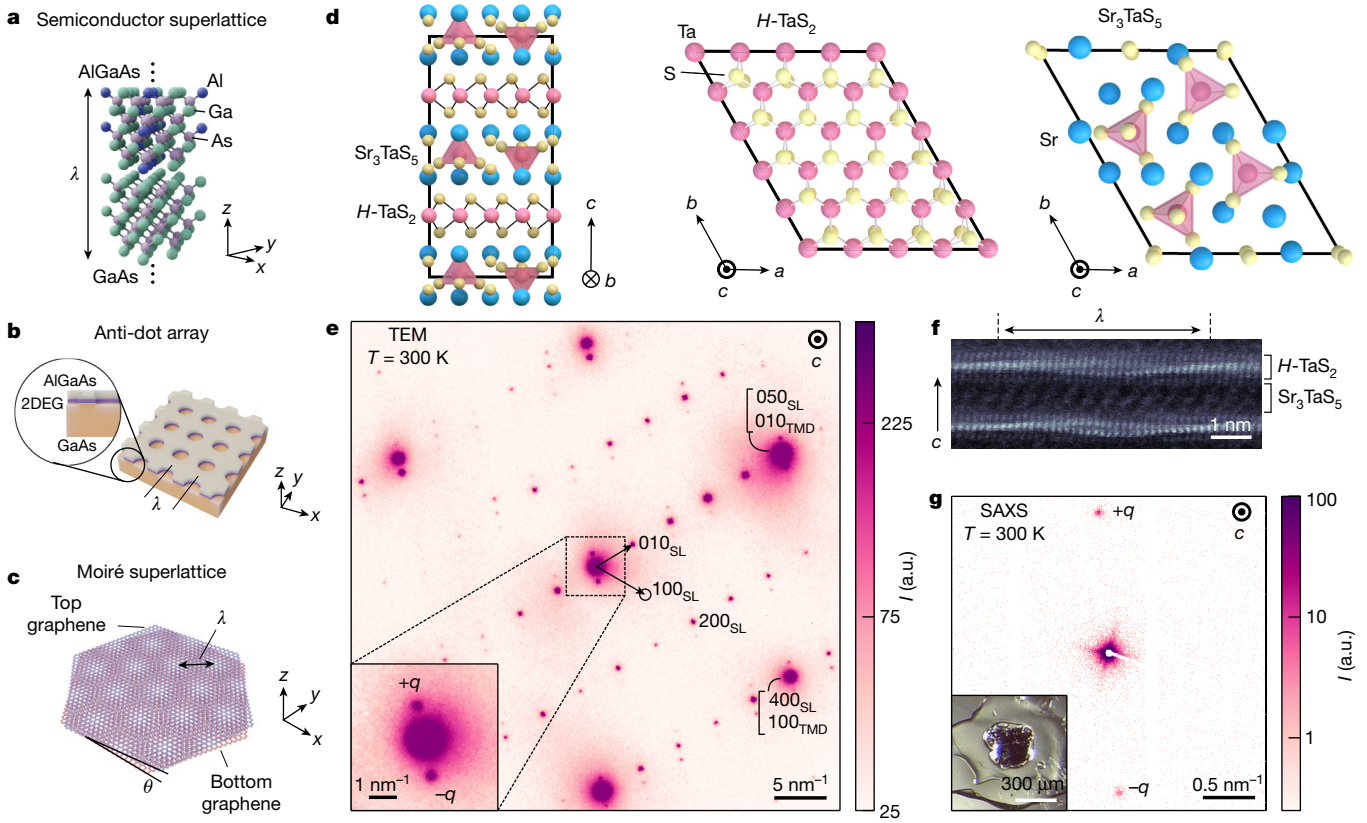

Fig. 1 | Periodically modulated crystals and a structurally modulated bulk superlattice. a, AlGaAs semiconductor superlattice with Al composition modulated with wavelength λ along the *c*-axis. **b**, 2DEG at AlGaAs–GaAs interface patterned with anti-dot array. **c**, Graphene layers rotationally misaligned by angle θ form a moiré pattern. **d**, Inversion symmetric stacking of Sr_3TaS_5 and *H*-TaS_2 in $SrTa_2S_5$ (average structure) (left). In-plane structures of *H*-TaS_2 TMD (middle) and Sr_3TaS_5 spacer layers (right). **e**, Electron diffraction pattern of the *ab*-plane at $T = 300$ K shows reflections from *H*-TaS_2 (hkl_{TMD}), Sr_3TaS_5 spacer layers (hkl_{SL}) and satellite reflections from a 1D structural modulation (inset). **f**, Real-space TEM cross-section showing out-of-plane structural modulation of *H*-TaS_2 layers. **g**, SAXS diffraction pattern in the *ab*-plane at $T = 300$ K shows satellite reflections from the structural modulation.

organic conductors[34], modulated bulk materials exhibit relatively low electronic mobilities (Methods).

Stripe-modulated metal

Here we report a bulk vdW superlattice[4,5,7,8] that naturally forms a macroscopically uniform incommensurate structural modulation with pronounced effects on its electronic behaviour. The material $SrTa_2S_5$ is composed of *H*-TaS_2 TMD and Sr_3TaS_5 spacer layers stacked in an alternating fashion (Fig. 1d, left). In the average structure, the latter has a two-fold symmetric in-plane structure (monoclinic point group 2) that forms a commensurate 4 × 5 superstructure with three-fold symmetric *H*-TaS_2 (hexagonal point group $\bar{6}m2$) (Fig. 1d, right, and Methods). Figure 1e shows an electron diffraction pattern of the *ab*-plane structure in which these features can be identified. We find dominant reflections from *H*-TaS_2 (Fig. 1e) and superstructure reflections from monoclinic Sr_3TaS_5 (Fig. 1e). We also observe satellite reflections at ±**q** (Fig. 1e, inset) from a long-wavelength 1D modulation. Using $|\mathbf{q}| = 2\pi/\lambda$, we estimate $\lambda \approx 4.4$ nm. The **q** vector has an irrational relationship with the reciprocal lattice of the average structure, demonstrating incommensuration (Extended Data Fig. 2b). High-resolution synchrotron powder X-ray diffraction shows the TMD layers are strained towards commensuration with the spacers to form the 4 × 5 superstructure (Extended Data Fig. 1f). This parallels misfit superlattices[35] and in-plane TMD heterointerfaces[36] in which translation symmetry mismatch gives rise to incommensurate structural modulations.

The 1D stripes are apparent in cross-section (Fig. 1f) and *ab*-plane (Extended Data Fig. 2a) transmission electron microscopy (TEM) images; the stripes are nearly perpendicular to the *a*-axis of the average structure (Methods). We observe an out-of-plane distortion of the *H*-TaS_2 layers with peak-to-valley amplitude $\delta z \approx 2.3$ Å and lateral periodicity of several nanometres, consistent with *ab*-plane electron diffraction. Cross-sectional electron diffraction indicates that this structural modulation is phase-shifted between adjacent layers (Extended Data Fig. 2c). Small-angle X-ray scattering (SAXS) at temperature $T = 300$ K from the *ab*-plane of bulk crystals (Fig. 1g, sample in inset) shows the same ±**q** pattern of satellite reflections with $\lambda = 4.385 \pm 0.015$ nm (Methods). Given the X-ray beam spot encompasses an area comparable to the measured crystals, the single pair of sharp ±**q** reflections demonstrate that the incommensurate structural modulation is macroscopically coherent. We propose that this large-scale coherence is rooted in the low symmetry of the average structure and the 1D nature of the modulation that restricts the allowed modulation directions (Methods).

Turning to the electronic properties of $SrTa_2S_5$, we examined the *T* dependence of in-plane resistivity perpendicular ($\rho_\perp$) and parallel ($\rho_\parallel$) to **q** using a focused ion beam (FIB) patterned L-bar device (Fig. 2a, inset). Similar to the parent TMD 2*H*-TaS_2, this system is a metal. Both $\rho_\perp(T)$ (Fig. 2a, orange and red) and $\rho_\parallel(T)$ (Fig. 2a, blue and green) show prominent thermal hysteresis in the range of 250 K < *T* < 350 K signalling a first-order phase transition. Although synchrotron powder X-ray diffraction, SAXS and electron diffraction do not indicate a structural transition, we find similar thermal hysteresis in torque magnetometry that points to an electronic origin (Extended Data Fig. 3a). Furthermore, first-principles calculations (Fig. 2c) show Fermi surface segments centred at B that are well-nested by the modulation *q*-vector (Fig. 2c, red). Together, these point to a first-order lock-in CDW transition as

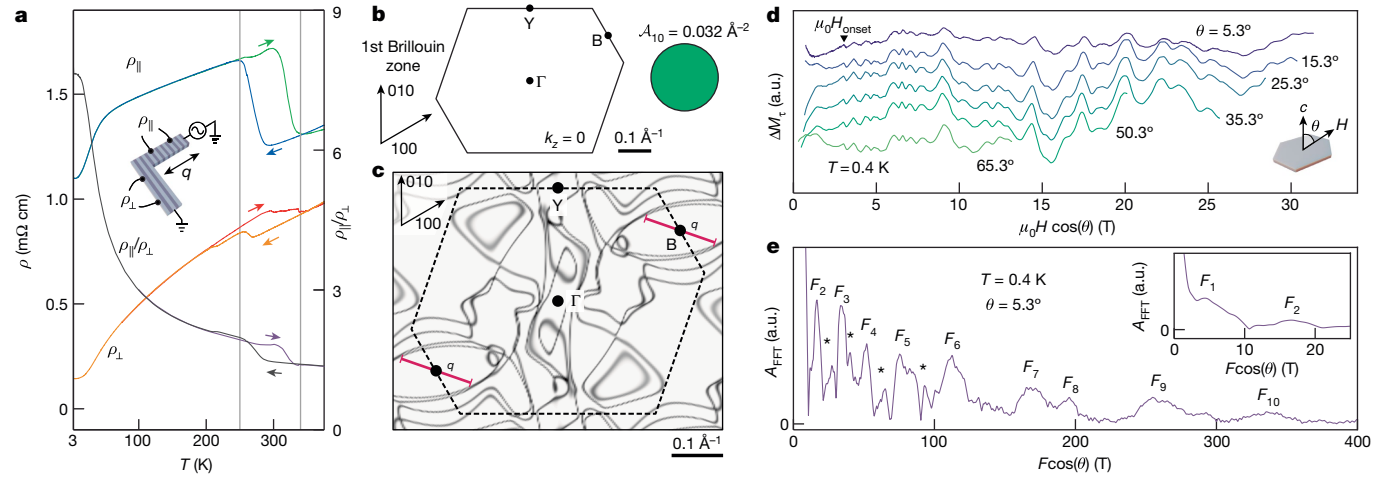

Fig. 2 | Transport anisotropy and fermiology of $SrTa_2S_5$. a, $\rho_\perp(T)$ (warming (red) and cooling (orange)), $\rho_\parallel(T)$ (warming (green) and cooling (blue)) and $\rho_\parallel/\rho_\perp(T)$ (warming (purple) and cooling (grey)) measured in an L-bar device (inset). **b**, Brillouin zone of $SrTa_2S_5$ with the Fermi surface cross-sectional area of $\mathcal{A}_{10}$ drawn to scale as a circle. **c**, First-principles calculation of the Fermi surfaces in the first Brillouin zone (dashed outline). The pocket centred at B is well-nested by the **q** vector (red) of the structural modulation. **d**, $\Delta M_\tau(H_\perp)$ with H inclined at various angles θ relative to the c-axis (inset) exhibit prominent dHvA quantum oscillations. **e**, FFT spectrum of $\Delta M_\tau(1/H_\perp)$ at $T = 0.4$ K and $\theta = 5.3°$ (axes are linear scale). Frequencies consistent with magnetic breakdown orbits are marked by stars (⋆). Inset, expanded view of FFT spectrum at low $F\cos(\theta)$.

the source of the thermal hysteresis (Methods). At lower T, the in-plane transport anisotropy $\rho_\parallel/\rho_\perp$ (Fig. 2a, grey and purple) increases and reaches $\rho_\parallel/\rho_\perp \approx 8$ at $T = 3$ K. Comparable $\rho_\parallel/\rho_\perp$ is found in the high-field nematic phase of 2DEGs[37], certain stripe-phase cuprates[38] and misfit superlattices[39], but markedly less than that of TMDs such as 1T'-WTe_2 with quasi-1D intralayer structures[40], which suggests the stripe modulation acts as a perturbation.

Quantum and commensurability oscillations

We also observe quantum oscillations in $SrTa_2S_5$ that enable us to map its fermiology. Figure 2d shows de Haas–van Alphen (dHvA) oscillations in torque magnetization $\Delta M_\tau(1/H_\perp)$ (Methods) at $T = 0.4$ K versus the magnetic field component perpendicular to the ab-plane, $H_\perp = H\cos\theta$, where H is the total field and θ is measured from the c-axis (Fig. 2d, inset). The alignment of $\Delta M_\tau(1/H_\perp)$ across various fixed θ indicates the Fermi surfaces are cylindrical and aligned along c because of weak interlayer coupling (Methods). The complex oscillatory behaviour of $\Delta M_\tau(H)$ is because of interference amongst numerous oscillation frequencies and corresponding Fermi surfaces. We extract the individual frequency F components from the fast Fourier transform (FFT) of $\Delta M_\tau(1/H_\perp)$. The FFT spectrum for $\theta = 5.3°$ and $T = 0.4$ K is shown in Fig. 2e, exhibiting numerous F components spanning $F_1 = 4.4$ T to $F_{10} = 335$ T (Methods), reflecting the complex electronic structure of $SrTa_2S_5$ (Fig. 2c). We also find weaker F contributions (Fig. 2e, starred) which we ascribe to magnetic breakdown between closely spaced Fermi surfaces (Methods), further consistent with the complex electronic structure (Fig. 2c). Comparison of the FFT spectra obtained at various θ also confirms the quasi-2D nature of the electronic structure (Extended Data Fig. 4e).

Using Onsager's relation[41] (Methods), we find the largest Fermi surface of $SrTa_2S_5$ encloses an area $\mathcal{A}_{10} = 0.032$ Å^{-2} (Fig. 2b) in the Brillouin zone, a factor of 10 smaller than anticipated for H-TaS_2 (Extended Data Fig. 4f,g). This is consistent with the zone folding of the H-TaS_2 Fermi surfaces into a nearly 20-fold smaller Brillouin zone of $SrTa_2S_5$ because of the 4 × 5 superlattice periodicity imposed by the spacer. More broadly, the appearance of quantum oscillations in this incommensurately

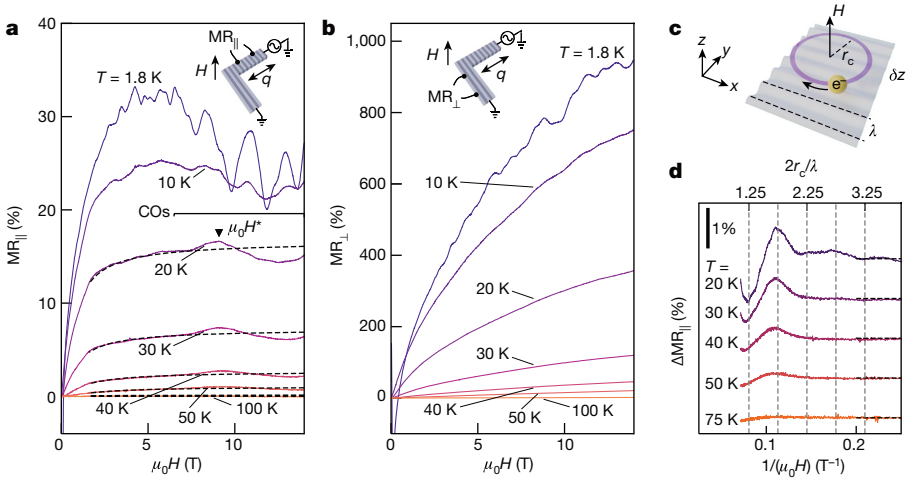

Fig. 3 | Semiclassical commensurability oscillations in a stripe-modulated superlattice. a,**b**, $MR_\parallel(H)$ (**a**) and $MR_\perp(H)$ (**b**) measured parallel and perpendicular to **q**, respectively, in a single FIB patterned device at various fixed T showing $1/H$ periodic oscillations. Oscillations persist in $MR_\parallel(H)$ to $T \approx 50$ K, which are absent in $MR_\perp(H)$, consistent with commensurability oscillations, labelled COs $\mu_0 H^*$ marks a peak in the COs found in $MR_\parallel$ (Extended Data Fig. 5c). **c**, Schematic of commensurability oscillations that arise because of commensuration between the cyclotron diameter $2r_c$ and the modulation wavelength λ. **d**, $\Delta MR_\parallel(1/H)$ at high T extracted by subtracting a monotonic background from $MR_\parallel$ (dashed lines in **a**), which shows commensurability oscillations with a characteristic 1/4 period phase shift.

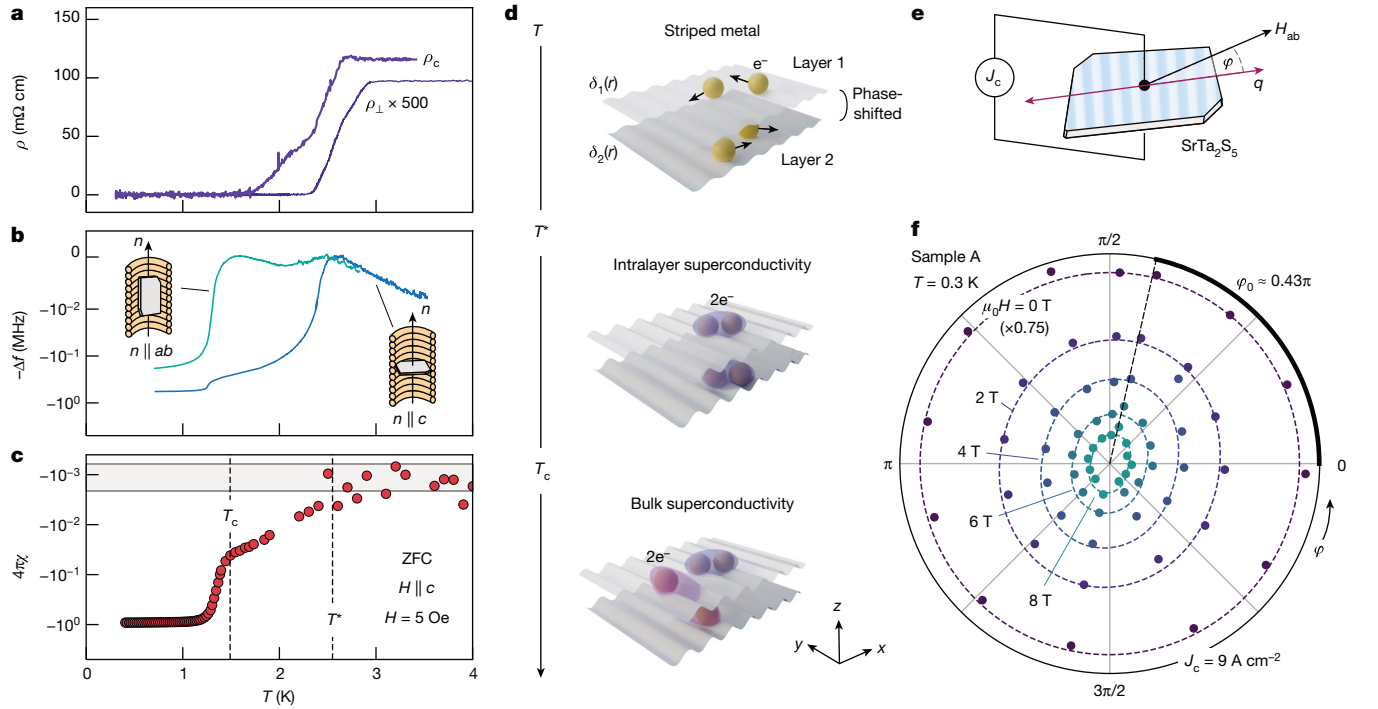

Fig. 4 | Superconductivity with suppressed interlayer coherence and in-plane anisotropy. a, Intralayer resistivity $\rho_\perp(T)$ measured perpendicular to the modulation **q** and interlayer resistivity $\rho_c(T)$ show a separation in T, at which they reach zero. **b**, Temperature dependence of tunnel diode oscillator frequency shift $-\Delta f(T)$ with c-axis (blue) and ab-plane (green) aligned with the coil axis n, respectively. Screening supercurrents, which are probed by Δf, onset at distinct T. **c**, Zero-field cooled (ZFC) magnetic susceptibility $4\pi\chi(T)$ measured for $H = 5$ Oe aligned with the c-axis exhibits weak screening for $T_c < T < T^\star$, followed by a bulk Meissner state for $T < T_c$. The grey box delineates the mean and standard deviation bounds of the normal state susceptibility, $\overline{\chi}(3\,\mathrm{K} < T < 5\,\mathrm{K}) \pm \sigma_\chi(3\,\mathrm{K} < T < 5\,\mathrm{K})$. **d**, Sequence of transitions found at low T in $SrTa_2S_5$, in which a striped metallic normal state gives way to intralayer superconductivity below $T^\star$, followed by bulk superconductivity at lower T_c. **e**,**f**, Experimental configuration (**e**) and polar plot (**f**) of interlayer critical current density J_c (sample A) versus in-plane magnetic field orientation $H_{ab}(\varphi)$ exhibiting prominent two-fold anisotropy.

modulated material is remarkable. From their onset field $\mu_0 H_{onset} \approx 3$ T (Fig. 2d, black triangle), we estimate a quantum mobility $\mu_q \approx 3{,}000$ cm^2 V^{-1} s^{-1}, markedly larger than mobilities seen in 2H-TaS_2 and H-TaS_2 containing misfit-layer compounds ($\mu \approx 1$ cm^2 V^{-1} s^{-1} and $\mu \approx 25$ cm^2 V^{-1} s^{-1}, respectively; Methods). Beyond presenting a bulk platform for exploring phase-coherent electrons in incommensurate potentials[42], the high quality of $SrTa_2S_5$ may support exotic but fragile modulated states[5].

The stripe modulation in $SrTa_2S_5$ leads to additional transport features characteristic of modulated 2DEGs. Figure 3a,b shows magnetoresistance measured parallel and perpendicular to **q**, $MR_{||}(H)$ and $MR_\perp(H)$, respectively (Methods). Together with Shubnikov–de Haas (SdH) oscillations paralleling dHvA oscillations in ΔM_τ, we find a low-frequency $F_{CO} \approx 15.5$ T oscillation in $MR_{||}$ that is absent in $MR_\perp$. Furthermore, this oscillation persists to $T > 50$ K, unlike dHvA oscillations that are suppressed by $T \approx 25$ K (Extended Data Fig. 4). The presence and absence of these oscillations in $MR_{||}$ and $MR_\perp$, respectively, indicate **q** of the stripes is relevant to their observation. The overall phenomenology parallels commensurability oscillations (COs) in stripe-patterned 2DEGs because of the matching of the cyclotron diameter $2r_c = 2\hbar k_F/(e\mu_0 H)$ and modulation λ (Fig. 3c) with frequency $F_{CO} = 2\hbar k_F/e\lambda$, where k_F is the Fermi wavevector[9,43]. Using the observed F_{CO} and $\lambda = 4.38$ nm from SAXS, we find $k_F \approx 6 \times 10^{-3}$ Å^{-1}, in nominal agreement with $k_F \approx 1 \times 10^{-2}$ Å^{-1} of the smallest pocket observed in dHvA oscillations (Methods). Moreover, these oscillations exhibit the characteristic 1/4 period phase shift anticipated for commensurability oscillations (ref. 44) (Fig. 3d) that is distinct from conventional quantum oscillations[41].

Hierarchy of superconducting transitions

At low T, superconductivity emerges from the stripe-modulated metallic state. Comparing the T dependence of intralayer (perpendicular to **q**) and interlayer resistivity, $\rho_\perp(T)$ and $\rho_c(T)$, respectively, we find ρ_c reaches zero at lower T relative to $\rho_\perp$ (Fig. 4a), suggesting suppressed interlayer coupling in the superconducting state. We also performed tunnel diode oscillator (TDO) measurements in this low T regime, in which the LC oscillator frequency f reflects changes in screening supercurrents[45,46] (Methods). The variation of f below $T = 2.5$ K, $\Delta f(T) = f(T) - f(2.5\,\mathrm{K})$ for crystals oriented with their c-axis or ab-plane parallel to the coil axis n, sensing the intralayer or interlayer supercurrent response, respectively, exhibit a similar hierarchy of T scales (Fig. 4b). For the same sample, we observe that intralayer screening onsets near 2.3 K (Fig. 4b, blue), whereas interlayer screening onsets near 1.4 K (Fig. 4b, green). Similar separation of T scales is observed in zero-field cooled magnetic susceptibility $\chi(T)$ for $H \,||\, c$: below $T^\star = 2.5$ K, where $\chi(T)$ crosses $\overline{\chi}(3\,\mathrm{K} < T < 5\,\mathrm{K}) \pm \sigma_\chi(3\,\mathrm{K} < T < 5\,\mathrm{K})$ (where $\overline{\chi}$ and σ_χ denote the mean and standard deviation, respectively), we observe weak diamagnetism consistent with the appearance of intralayer supercurrents (Fig. 4c), followed by a Meissner transition at $T_c = 1.49$ K with a shielding fraction $4\pi\chi \approx -1$ characteristic of bulk superconductivity (Methods). These observations establish that on cooling, intralayer superconducting coherence emerges from the striped metallic state below $T^\star$ followed by interlayer coherence at T_c (Fig. 4d). A possible origin is the large physical separation between H-TaS_2 layers in $SrTa_2S_5$ compared with 2H-TaS_2 with correspondingly weakened Josephson coupling[47]. However, when compared with related materials such as the superlattice $Ba_6Nb_{11}S_{28}$ (ref. 5) and the organic intercalated TMD $(pyridine)_{1/2}TaS_2$ (ref. 48), the degree to which interlayer coupling is frustrated in $SrTa_2S_5$ appears unusual. In particular, similar to $SrTa_2S_5$, $Ba_6Nb_{11}S_{28}$ and $(pyridine)_{1/2}TaS_2$ host superconducting TMD layers spaced approximately 12 Å apart by insulating spacer blocks. Although these related materials exhibit signatures of 2D superconductivity[5,48], they do not show the marked energetic

separation between intralayer and interlayer coherence found in $SrTa_2S_5$, suggesting large interlayer spacing is insufficient.

Instead, this sequence of transitions closely resembles that found in striped cuprate superconductors such as $La_{1.875}Ba_{0.125}CuO_4$ (refs. 15,17). In these systems, interlayer coherence is thought to be suppressed by pair-density wave (PDW) superconductivity with spatially modulated superconducting order (see also ref. 49) that is mismatched between adjacent CuO_2 layers[16]. Electron diffraction from the structural stripe modulation of $SrTa_2S_5$ indicates that it is phase-shifted between adjacent *H*-TaS_2 layers (Extended Data Fig. 2c), which, through coupling between the structural stripe and superconducting orders[50], could seed mismatched PDW order in adjacent *H*-TaS_2 layers (Methods). Early proposals predict that mismatched 1D PDW order, and correspondingly frustrated interlayer coupling, can be tuned using an in-plane magnetic field H_{ab} (refs. 12,13): H_{ab} perpendicular to **q** provides a momentum boost parallel to **q** that can compensate for the PDW mismatch, which can be sensed in the H_{ab} magnitude and orientation φ dependence of interlayer critical current density J_c (see schematic in Fig. 4e). As shown in Fig. 4f, the H_{ab} dependence of J_c exhibits a prominent two-fold anisotropy consistent with these predictions (Methods). Explaining the microscopic origins of this anisotropy in terms of intrinsic modulated superconductivity, anisotropic pinning of Josephson vortices and related effects (Methods) could pave the way towards a straightforward, global test for PDW order.

Perspective

The homogeneity of the incommensurate modulation and high degree of structural perfection exhibited by $SrTa_2S_5$ (it is in the clean limit of superconductivity; Methods) positions it within the reach of local scanning probes[18–21], macroscopic scattering experiments[22,23] and vdW device fabrication techniques to further probe the PDW order[12,13]. More broadly, the rich sequence of transitions found in this system stemming from the incommensurate stripe modulation demonstrates the versatility of this growing family of bulk vdW superlattices[5,7] to explore modulated electronic phases, potentially charting a path towards scaling moiré heterostructures and their analogues up to macroscopic scales.

Online content

Any methods, additional references, Nature Portfolio reporting summaries, source data, extended data, supplementary information, acknowledgements, peer review information; details of author contributions and competing interests; and statements of data and code availability are available at https://doi.org/10.1038/s41586-024-07589-5.

1. Cummins, H. Z. Experimental studies of structurally incommensurate crystal phases. *Phys. Rep.* **185**, 211–409 (1990).
2. Bistritzer, R. & MacDonald, A. H. Moiré bands in twisted double-layer graphene. *Proc. Natl Acad. Sci. USA.* **108**, 12233–12237 (2011).
3. Cao, Y. et al. Correlated insulator behaviour at half-filling in magic-angle graphene superlattices. *Nature* **556**, 80–84 (2018).
4. Hu, C. et al. A van der Waals antiferromagnetic topological insulator with weak interlayer magnetic coupling. *Nat. Commun.* **11**, 97 (2020).
5. Devarakonda, A. et al. Clean 2D superconductivity in a bulk van der Waals superlattice. *Science* **370**, 231–236 (2020).
6. Devarakonda, A. et al. Signatures of bosonic Landau levels in a finite-momentum superconductor. *Nature* **599**, 51–56 (2021).
7. Ma, K. et al. Two-dimensional superconductivity in a bulk superlattice van der Waals material $Ba_6Nb_{11}Se_{28}$. *Phys. Rev. Mater.* **6**, 044806 (2022).
8. Persky, E. et al. Magnetic memory and spontaneous vortices in a van der Waals superconductor. *Nature* **607**, 692–696 (2022).
9. Gerhardts, R. R., Weiss, D. & Klitzing, K. V. Novel magnetoresistance oscillations in a periodically modulated two-dimensional electron gas. *Phys. Rev. Lett.* **62**, 1173–1176 (1989).
10. Ensslin, K. & Petroff, P. M. Magnetotransport through an antidot lattice in GaAs-$Al_xGa_{1-x}As$ heterostructures. *Phys. Rev. B* **41**, 12307–12310 (1990).
11. Huber, R. et al. Band conductivity oscillations in a gate-tunable graphene superlattice. *Nat. Commun.* **13**, 2856 (2022).
12. Yang, K. Detection of striped superconductors using magnetic field modulated Josephson effect. *J. Supercond. Nov. Magn.* **26**, 2741–2742 (2013).
13. Yang, K. & Agterberg, D. F. Josephson effect in Fulde-Ferrell-Larkin-Ovchinnikov superconductors. *Phys. Rev. Lett.* **84**, 4970–4973 (2000).
14. Lozano, P. M. et al. Testing for pair density wave order in $La_{1.875}Ba_{0.125}CuO_4$. *Phys. Rev. B* **106**, 174510 (2022).
15. Li, Q., Hücker, M., Gu, G. D., Tsvelik, A. M. & Tranquada, J. M. Two-dimensional superconducting fluctuations in stripe-ordered $La_{1.875}Ba_{0.125}CuO_4$. *Phys. Rev. Lett.* **99**, 067001 (2007).
16. Berg, E. et al. Dynamical layer decoupling in a stripe-ordered high-T_c superconductor. *Phys. Rev. Lett.* **99**, 127003 (2007).
17. Tranquada, J. M. Cuprate superconductors as viewed through a striped lens. *Adv. Phys.* **69**, 437–509 (2020).
18. Liu, X., Chong, Y. X., Sharma, R. & Davis, J. C. S. Discovery of a Cooper-pair density wave state in a transition-metal dichalcogenide. *Science* **372**, 1447–1452 (2021).
19. Gu, Q. et al. Detection of a pair density wave state in UTe_2. *Nature* **618**, 921–927 (2023).
20. Zhao, H. et al. Smectic pair-density-wave order in $EuRbFe_4As_4$. *Nature* **618**, 940–945 (2023).
21. Liu, Y. et al. Pair density wave state in a monolayer high-T_c iron-based superconductor. *Nature* **618**, 934–939 (2023).
22. Tranquada, J. M., Sternlieb, B. J., Axe, J. D., Nakamura, Y. & Uchida, S. Evidence for stripe correlations of spins and holes in copper oxide superconductors. *Nature* **375**, 561–563 (1995).
23. Valla, T., Fedorov, A. V., Lee, J., Davis, J. C. & Gu, G. D. The ground state of the pseudogap in cuprate superconductors. *Science* **314**, 1914–1916 (2006).
24. Axe, J. D., Mason, R., Mitchell, E. W. J. & White, J. W. Incommensurate structures. *Philos. Trans. R. Soc. Lond. B Biol. Sci.* **290**, 593–603 (1980).
25. Overhauser, A. W. Exchange and correlation instabilities of simple metals. *Phys. Rev.* **167**, 691–698 (1968).
26. Izyumov, Y. A. Modulated, or long-periodic, magnetic structures of crystals. *Sov. Phys. Usp.* **27**, 845–867 (1984).
27. Dresselhaus, M. S. (ed.) *Intercalation in Layered Materials* (Springer, 1986).
28. Monceau, P. Electronic crystals: an experimental overview. *Adv. Phys.* **61**, 325–581 (2012).
29. de Wolff, P. M., Janssen, T. & Janner, A. The superspace groups for incommensurate crystal structures with a one-dimensional modulation. *Acta Crystallogr. A* **37**, 625–636 (1981).
30. Esaki, L. & Tsu, R. Superlattice and negative differential conductivity in semiconductors. *IBM J. Res. Dev.* **14**, 61–65 (1970).
31. Esaki, L. & Chang, L. L. New transport phenomenon in a semiconductor "superlattice". *Phys. Rev. Lett.* **33**, 495–498 (1974).
32. Serlin, M. et al. Intrinsic quantized anomalous Hall effect in a moiré heterostructure. *Science* **367**, 900–903 (2020).
33. Li, T. et al. Quantum anomalous Hall effect from intertwined moiré bands. *Nature* **600**, 641–646 (2021).
34. Kawamoto, T. & Takimiya, K. Organic superconductors with an incommensurate anion structure. *Sci. Technol. Adv. Mater.* **10**, 024303 (2009).
35. Kuypers, S., Van Tendeloo, G., Van Landuyt, J. & Amelinckx, S. The incommensurate misfit layer structure of $(SnS)_{1.17}NbS_2$, '$SnNbS_2$'. II. A study by means of electron microscopy. *Acta Crystallogr. A* **45**, 291–296 (1989).
36. Xie, S. et al. Coherent, atomically thin transition-metal dichalcogenide superlattices with engineered strain. *Science* **359**, 1131–1136 (2018).
37. Fradkin, E., Kivelson, S. A., Manousakis, E. & Nho, K. Nematic phase of the two-dimensional electron gas in a magnetic field. *Phys. Rev. Lett.* **84**, 1982–1985 (2000).
38. Ando, Y., Segawa, K., Komiya, S. & Lavrov, A. N. Electrical resistivity anisotropy from self-organized one dimensionality in high-temperature superconductors. *Phys. Rev. Lett.* **88**, 137005 (2002).
39. Sakabayashi, H. & Okazaki, R. Crossover from itinerant to localized states in the thermoelectric oxide $[Ca_2CoO_3]_{0.62}[CoO_2]$. *Phys. Rev. B* **103**, 125119 (2021).
40. Jha, R. et al. Anisotropy in the electronic transport properties of Weyl semimetal WTe_2 single crystals. *AIP Adv.* **8**, 101332 (2018).
41. Shoenberg, D. *Magnetic Oscillations in Metals* (Cambridge Univ.Press, 1984).
42. Spurrier, S. & Cooper, N. R. Theory of quantum oscillations in quasicrystals: quantizing spiral Fermi surfaces. *Phys. Rev. B* **100**, 081405 (2019).
43. Beenakker, C. W. J. Guiding-center-drift resonance in a periodically modulated two-dimensional electron gas. *Phys. Rev. Lett.* **62**, 2020–2023 (1989).
44. Winkler, R. W., Kotthaus, J. P. & Ploog, K. Landau band conductivity in a two-dimensional electron system modulated by an artificial one-dimensional superlattice potential. *Phys. Rev. Lett.* **62**, 1177–1180 (1989).
45. Schawlow, A. L. & Devlin, G. E. Effect of the energy gap on the penetration depth of superconductors. *Phys. Rev.* **113**, 120–126 (1959).
46. Giannetta, R., Carrington, A. & Prozorov, R. London penetration depth measurements using tunnel diode resonators. *J. Low Temp. Phys.* **208**, 119–146 (2022).
47. Klemm, R. A., Luther, A. & Beasley, M. R. Theory of the upper critical field in layered superconductors. *Phys. Rev. B* **12**, 877–891 (1975).
48. Gamble, F. R. et al. Intercalation complexes of Lewis bases and layered sulfides: a large class of new superconductors. *Science* **174**, 493–497 (1971).
49. Agosta, C. C. Inhomogeneous superconductivity in organic and related superconductors. *Crystals* **8**, 285 (2018).
50. Fradkin, E., Kivelson, S. A. & Tranquada, J. M. *Colloquium*: Theory of intertwined orders in high temperature superconductors. *Rev. Mod. Phys.* **87**, 457–482 (2015).

Methods

Single-crystal synthesis and characterization

Single crystals of $SrTa_2S_5$ were grown from a powder mixture of SrS, Ta and S in the presence of anhydrous $SrCl_2$. SrS, Ta, S and anhydrous $SrCl_2$ (all purities ≥99.99%) were combined in the molar ratio 1:1:2:0.25 under argon in a glove box. The mixture was subsequently sealed in an evacuated quartz ampoule and heated at 1,050 °C for more than 120 h followed by cooling at 2 °C h^{-1} to 750 °C and furnace cooling to room temperature. This procedure resulted in thin, lustrous black plates with typical dimensions of 0.4 × 0.4 × 0.03 mm^3 (length × width × thickness). Care is taken to minimize the exposure of crystals to solvents. Synthesized crystals were stored under vacuum before characterization.

The crystal structure was analysed by powder X-ray diffraction (PXRD), SAXS, electron diffraction and high-angle annular dark-field scanning transmission electron microscopy (HAADF-STEM). In-house PXRD was performed using a commercial diffractometer with a Cu source. High-resolution synchrotron PXRD data were collected at beamline 11-BM at the Advanced Photon Source, Argonne National Laboratory, at an average $\lambda = 0.458104$ Å. Samples for in-house and synchrotron PXRD were prepared by grinding crystals together with amorphous silica to mitigate preferred orientation effects and reduce absorption by the heavy constituent elements.

SAXS experiments were performed in a transmission geometry using a commercial SAXSLAB system equipped with a variable temperature sample holder (T = 400 K to 100 K). Samples were affixed to thin mica membranes using a small amount of GE varnish. We used an X-ray beam spot approximately 250 μm in diameter for all measurements. The uncertainty in computing λ is because of the misalignment of the sample c-axis with respect to the incoming beam, which makes $|+\mathbf{q}| \neq |-\mathbf{q}|$.

HAADF-STEM experiments were conducted at a CEOS Cs probe corrected cold emission gun JEOL JEM-ARM200F STEM operated at 200 kV acceleration voltage. HAADF-STEM images were acquired with 75 mrad convergence semi-angle and 2D Wiener filter applied to reduce the noise. Samples were prepared by an FEI Helios FIB, operated at 30 kV acceleration voltage for the gallium beam during lift-out and 2 kV during polishing. Additional polishing was performed at 0.5 kV with a Fischione NanoMill for 10 min on each side at a milling angle of ±10°.

Transport measurements and FIB transport sample preparation

Longitudinal and transverse resistivity were measured using standard a.c. lock-in techniques. Longitudinal (transverse) voltages were (anti-) symmetrized to correct for contact misalignment. We compute $MR_{\perp}(H)$ and $MR_{||}(H)$ for $T < 3$ K using $\rho_{\perp}(0)$ and $\rho_{||}(0)$ in the normal state at $T = 3$ K. Current–voltage (I–V) characteristics were measured in a four-probe configuration. The sample was voltage-biased (Yokogawa GS200) and the resulting current was measured using a current pre-amplifier (DL Instruments Model 1211). The longitudinal voltage was simultaneously measured using a Keithley 2182 A nanovoltmeter. Up- and down-sweep I–V traces were coincident, which indicates Joule heating is minimal.

L-bar devices for transport anisotropy measurements were prepared using an FEI Helios FIB system (gallium ion source) operating at 30 kV. Coarse milling was performed using a 10-nA beam current followed by side-wall polishing using a 1-nA beam current.

Average model structure

To examine the structure of this large unit cell, modulated system, we follow approaches established for misfit TMD superlattices[35], in which we first construct an average model structure without the modulation. We then consider perturbations to the structure by the incommensurate modulation. We used a combination of real-space imaging by HAADF-STEM and reciprocal space imaging by electron diffraction, PXRD and SAXS to construct this model. Together these techniques provide structural information spanning local (about 100 nm for HAADF-STEM and electron diffraction) to macroscopic length scales (around 100 μm for SAXS and PXRD).

In TEM cross-section images (Fig. 1f), we see two types of distinct layer. As described in the following, we identify the brighter, more atomically dense layer as a TMD (H-TaS_2) and the dimmer, sparser layer as a spacer giving rise to the 4 × 5 superstructure reflections. By examining diffraction patterns collected by looking along the in-plane direction (Extended Data Fig. 2c), we find the lattice constant along the stacking direction to be approximately 25 Å (this is consistent with the PXRD unit cell, described below). Comparing this with real-space imaging of the cross-section (Fig. 1f), we see that this requires there to be two TMD and two spacer layers in the unit cell. The modulation (wavelength λ) is also evident in Fig. 1f, which we return to below.

TEM diffraction along the [001] direction (Fig. 1e) shows strong reflections forming a hexagonal motif, spacer layer reflections with two-fold symmetry and weaker satellite reflections from the structural modulation. We extract the peak positions of the strong reflections by least-squares fitting each to a 2D Gaussian profile (Extended Data Fig. 1a, red points). The average angle between adjacent reflections is $\phi = 60 \pm 0.9°$, indicating that, within our resolution, the reflections originate from a hexagonal lattice. The corresponding magnitude of the reciprocal lattice vector is $|\mathbf{q}| = 2.26 \pm 0.03$ Å^{-1}. This can be used to extract the real-space lattice constant a_{TMD} using $|\mathbf{q}| = 4\pi/(\sqrt{3}a_{TMD})$ for hexagonal systems; we find $a_{TMD} = 3.21 \pm 0.09$ Å, which is consistent with the in-plane lattice constant $a_{TMD} = 3.314$ Å of H-TaS_2 layers in bulk $2H$-TaS_2 (ref. 51). This is the smallest periodicity in the system as the superlattice and satellite reflections have smaller $|\mathbf{q}|$.

To determine the structural relationship between the spacer and TMD layers, we take linecuts of the electron diffraction patterns along the (100) and (010) reciprocal lattice directions (Extended Data Fig. 1a, blue and green dashed lines, respectively). Along the (100) direction, we find a superstructure reflection halfway between the zone centre and the 100_{TMD} reflection (Extended Data Fig. 1b). We identify this as the 200_{SL} reflection of the spacer layer with a systematic absence of the odd 100_{SL} and 300_{SL} reflections (Extended Data Fig. 1b, open triangles). This corresponds to a spacer layer with a four times larger real-space lattice constant relative to H-TaS_2 along the real-space [100] direction. A linecut along the (010) direction shows superstructure reflections at one-fifth intervals relative to the 010_{TMD} reflection (Extended Data Fig. 1c), indicating a five times larger real-space lattice constant relative to H-TaS_2 in this direction. This is the minimum size needed to accommodate a spacer layer motif similar to that of $Ba_6Nb_{11}S_{28}$ (ref. 5) and is consistent with the observed zone folding of the electronic structure (see below).

The linecut analysis shows a spacer layer structure that leads to a 4 × 5 in-plane superstructure with respect to the TMD layer; this superstructure has two-fold symmetry. Together with the systematic absence of $h00_{SL}$ reflections with odd h, this requires the average model structure to occupy a monoclinic space group with a non-symmorphic symmetry—that is, glide and/or screw operation along the real-space $[100]_{SL}$ direction. These conditions are satisfied by the space group $P112_1/a$ (No. 14 with c-axis unique), which possesses the highest point group symmetry allowed for monoclinic systems. The highest symmetry model structure in this space group (Fig. 1d) has a composition $SrTa_2S_5$ with spacer composition Sr_3TaS_5 and TMD composition TaS_2. This average model structure is consistent with in-house and synchrotron PXRD patterns (Extended Data Fig. 1d). We extract the lattice constants for this model using the PXRD pattern and find $a = 13.17$ Å, $b = 16.47$ Å, $c = 24.81$ Å and $\gamma = 120°$ at $T = 300$ K, which are comparable to those from electron diffraction. The model structure and lattice parameters at $T = 300$ K are provided in Extended Data Table 1. We also examined the temperature dependence of synchrotron PXRD. Cooling from $T = 300$ K to 100 K, we find the observed reflections are nearly invariant (Extended Data Fig. 1d,e), demonstrating that the symmetries of the structure do not change across this T range. Instead, we find a

systematic increase in $1/d$ of the reflections with decreasing T, which is consistent with the thermal contraction of the unit cell.

This structure has lower symmetry relative to bulk 2*H*-TaS_2 because of the monoclinic spacer; the allowed symmetry operations are 1, $\bar{1}$, $\{2_{001} \mid ½\ 0\ ½\}$ and $\{m_{001} \mid ½\ 0\ ½\}$. Overall, the structure preserves the inversion symmetric stacking of TMD monolayers in bulk 2*H*-TaS_2. The *H*-TaS_2 layers intrinsically break inversion symmetry, which, together with the absence of a mirror symmetry across the *ab*-plane, produces a locally polar environment for the *H*-TaS_2 layers. In the limit of weak interlayer coupling in which local symmetry breaking can play an important part, this could support a variety of new electronic orders that could be further enriched by the strong spin–orbit coupling (SOC) of TMDs[52,53].

Incommensurate modulation

We now consider how the modulation arises from this average model structure. Examination of the in-plane reflections by high-resolution synchrotron PXRD at $T = 300$ K shows a splitting between the 400, $4\bar{5}0$ and 050 peaks (Extended Data Fig. 1e). This points to in-plane strain in the *H*-TaS_2 layer that makes the hexagonal in-plane principal axes inequivalent; the observed splitting is consistent with compressive (−0.2%) and tensile (+0.2%) strain along the *a*- and *b*-axes, respectively, relative to the average model structure. The symmetric splitting of the 400 and 050 reflections about the $4\bar{5}0$ peak indicates that the angle γ between the *a*- and *b*-axes remains 120°. This splitting in the PXRD pattern is qualitatively similar at lower $T = 100$ K, except that the reflections move to higher $1/d$, consistent with thermal contraction of the unit cell discussed above. This strain configuration of the *H*-TaS_2 layer is shown in Extended Data Fig. 1f.

It is observed in electron diffraction (Fig. 1e and Extended Data Fig. 1a) that the modulation **q** is parallel to the $(1\bar{1}0)_{SL}$ reciprocal lattice direction. In real space, this translates to the modulation being in close alignment with the *a*-axis (Extended Data Fig. 1f), suggesting the compressive strain along the *a*-axis observed by PXRD primarily drives the out-of-plane corrugation associated with **q**. This out-of-plane corrugation is also observed in TEM images of the *ab*-plane atomic structure of the TMD layer (Extended Data Fig. 2a). To establish incommensuration with respect to the atomic lattice, we perform a linecut analysis of the electron diffraction pattern along the reciprocal $(1\bar{1}0)_{SL}$ direction (Extended Data Fig. 1a, dashed red line), the results of which are shown in Extended Data Fig. 2b.

We see that the $(2\bar{2}0)_{SL}$ reflection does not align with integer multiples of the modulation **q**, establishing their incommensuration. Furthermore, the absence of higher harmonic reflections of ±**q** indicates the modulation is relatively weak and does not induce charge localization as seen in, for example, stripe-ordered nickelates[54]. Electron diffraction from the cross-section of $SrTa_2S_5$ exhibits an extinction condition for the $\pm q0n$ for odd n (Extended Data Fig. 2c) satellite reflections from the incommensurate modulation. Given the average unit cell contains two *H*-TaS_2 layers, the highest symmetry structure that satisfies this extinction condition relates the modulation in adjacent *H*-TaS_2 by a two-fold screw axis aligned to *c*; this is also equivalent to a π phase shift of the modulation between adjacent layers.

The incommensurate relationship between the modulation and the average structure indicates that three-dimensional (3D) translational symmetry is strictly absent. This poses an impediment to the first-principles electronic structure calculations. Although this issue is avoided in the recently studied moiré systems by continuum models[2], the metallic nature of the *H*-TaS_2 layers makes this impractical because of the many bands at the Fermi level. An alternative approach often used to study quasicrystals, which also lack 3D translational symmetry, is to construct an approximant crystal structure that mimics the incommensurately modulated structure. Extended Data Fig. 2d shows an approximant (a_{approx}, b_{approx} and c_{approx} are the principal axes of the approximant unit cell), in which the $(2\bar{2}0)_{SL}$ reflection of the average structure and 7**q** are forced to coincide, recovering translation symmetry. Furthermore, adjacent TMD layers are related by a π phase shift along the a_{approx} axis. First-principles calculations of these systems are possible, although these calculations become computationally expensive because of the greatly expanded unit cell of the approximant structure.

SAXS experiments establish that this incommensurate modulation can be coherent across macroscopic length scales comparable to the crystal size (Fig. 1g). This is in contrast to some incommensurately modulated bulk systems in which the modulation exhibits disorder at these length scales. For example, the layered cuprate $Bi_2Sr_2CaCu_2O_{8+\delta}$, which also manifests an in-plane 1D incommensurate modulation, exhibits domains between which the modulation direction is rotated by 90° (ref. 55). This stems from its near-perfect tetragonal symmetry that permits twin domains with interchanged *a*- and *b*-axes. The monoclinic point group symmetry of $SrTa_2S_5$ with both disparate *a* and *b* lattice constants and γ far from 90° (monoclinic, *c*-axis unique) makes twinning unfavourable[56]. We propose that the out-of-plane corrugation is driven by the *a*-axis compression that may act to constrain the modulation **q** towards this direction. Some samples produce SAXS patterns with multiple **q** directions (see, for example, Extended Data Fig. 2e); however, they are not related by rotational symmetry and are probably because of the fusing of multiple single crystals with polycrystalline matter.

We propose that the mechanism driving the incommensurate structural modulation parallels that of lateral TMD heterointerfaces[36] and vdW moiré systems[57–59]. In both of these contexts, they develop periodic, long-wavelength out-of-plane corrugations to form energetically favourable, locally commensurate structures that mitigate mismatched translation symmetries. In $SrTa_2S_5$, the TMD layer is strained in the plane (Extended Data Fig. 1f) to form a commensurate 4 × 5 superstructure with the spacer. Consequently, it develops the observed incommensurate stripe modulation with out-of-plane corrugations. The peak-to-peak amplitude of the out-of-plane distortion observed for the *H*-TaS_2 layers is approximately 2.3 Å (Fig. 1f), which is comparable to that observed in the lateral TMD heterointerfaces[36]. This reinforces the idea that the energetic favourability of locally commensurate structures with a trade-off in out-of-plane distortion (relatively low cost energetically for the vdW layers) is the driving mechanism. This also suggests that further strain engineering at the spacer–TMD interface could realize 2D modulated phases similar to vdW moiré systems but with macroscopic coherence across bulk crystals.

Evidence for lock-in charge-density wave

The thermal hysteresis seen in electrical transport between 250 K < T < 350 K (Fig. 2a) is suggestive of a phase transition. We performed additional thermodynamic and structural characterization to determine the origin of this transition. Extended Data Fig. 3a shows the magnetic torque τ response of $SrTa_2S_5$, detected using a capacitive cantilever, as a function of T at fixed $\mu_0 H = 1$ T applied at an angle $\theta = 15°$ relative to the *c*-axis (Extended Data Fig. 3a, inset). In this configuration, the parallel plate capacitance C_τ is proportional to $|\boldsymbol{\tau}|$, where $\boldsymbol{\tau} = \mathbf{M} \times \mathbf{H}$.

Paralleling the transport results, we observe thermal hysteresis in $C_\tau(T)$ between cooling and warming in this T range (Extended Data Fig. 3a). To determine the T span of the hysteresis loop, we examine the derivative $\partial C_\tau / \partial T$ for various fixed $\mu_0 H$ (Extended Data Fig. 3b). Across the measured values of $\mu_0 H$, we find the loop spans 210 K < T < 360 K, in nominal agreement with the transport results. The fact that the hysteresis T range is invariant with H suggests that the thermal hysteresis is not magnetic in nature. Furthermore, the fact that synchrotron PXRD does not evidence symmetry breaking on cooling from 300 K to 100 K disfavours a structural origin to the hysteresis. Together, the transport and torque measurements suggest that this transition is electronic in origin. The propensity of TMDs to form charge-density wave (CDW) order[60] suggests that this hysteresis is linked to emergent CDW order

in the H-TaS_2 layers of $SrTa_2S_5$. Given CDW order can give rise to new superlattice diffraction peaks, we performed SAXS measurements at various fixed T cooling from 400 K to 100 K (Extended Data Fig. 3c). The absence of new reflections in the SAXS patterns is suggestive of a lock-in CDW in which the CDW periodicity follows the underlying structural modulation; such lock-in transitions have been observed in other TMDs[61].

We find further evidence in the first-principles calculations that a lock-in transition is favourable. We performed electronic structure calculations implemented in the Vienna ab initio simulation package[62,63] using the projector augmented wave pseudo-potential method[64] and exchange–correlation functional in the generalized gradient approximation parametrized by Perdew–Burke–Ernzerhof[65]. Examining the calculated Fermi surfaces, we find portions that are well-nested by the modulation $\mathbf{q}$ (Fig. 2c), suggesting the lock-in CDW is energetically favourable[61]. This is more easily visualized by computing the auto-correlation $M(\mathbf{k}) = A(\mathbf{k}) \times A(\mathbf{k}+\mathbf{q})$, where $A(\mathbf{k})$ is the Fermi surface spectral function intensity at $\mathbf{k}$ in reciprocal space. We focus on the $SrTa_2S_5$ Fermi surfaces originating from the K/K′ point bands of H-TaS_2 before zone folding (isolated by band unfolding and projecting the electronic structure of $SrTa_2S_5$ onto the H-TaS_2 bands (Extended Data Fig. 3d); ref. 66), as these are the Fermi surfaces that exhibit nesting with $\mathbf{q}$. Extended Data Fig. 3e shows $M(\mathbf{k})$ obtained from these Fermi surfaces, which exhibits a hotspot at $\mathbf{k} \approx \mathbf{q}$ characteristic of Fermi surface nesting. Similar to early work on TMDs, scanning tunnelling microscopy (STM) could probe the modulated electron density characteristic of the lock-in CDW[67]. Moreover, the connection between this transition and the incommensurate structural modulation suggests that strain could be a powerful tuning parameter for further exploring its behaviour. Suppressing the transition temperature into the regime in which quantum oscillations are observable could enable a probe of this phenomenon. High-precision measurements of specific heat could also provide additional thermodynamic insight into this transition.

Quantum oscillations and fermiology

We observe quantum oscillations in torque magnetization $M_\tau = (\tau(H) - \tau(0))/(\mu_0 H \sin\theta)$, where τ is measured by a piezoresistive cantilever (Seiko PRC-400 and SCL Sensortech PRSA-L300). The piezoresistive elements, one with sample mounted and the other empty for reference, were incorporated into a Wheatstone bridge and balanced at zero field. The torque signal was detected using standard a.c. lock-in techniques with excitations below 20 mV across the bridge. A co-mounted Hall sensor was used to calibrate the rotation angle.

We extract the oscillatory component $\Delta M_\tau(H)$ by removing a polynomial background obtained by least-squares fitting in the field region $0.75\ \mathrm{T} < \mu_0 H < 31\ \mathrm{T}$. This is illustrated for oscillations in $M_\tau(H)$ at various fixed T and $\theta = 25.3°$ (Extended Data Fig. 4a, vertically offset for clarity) with background shown as black dashed lines. We extract quantum oscillation frequencies F from $\Delta M_\tau(1/H)$ using an FFT; Fig. 2e shows the FFT spectrum for $\theta = 5.3°$ and $T = 0.4$ K. The corresponding Fermi surface areas $\mathcal{A}$ are obtained from the FFT frequencies using Onsager's relation, $F = \hbar\mathcal{A}/2\pi e$ (ref. 68) (Extended Data Table 2). In between these primary frequencies in the FFT, we find weaker peaks at $F = 27.2$ T, 40.2 T, 64.8 T and 92.8 T. The reduced amplitude of these contributions suggests that these peaks originate from a magnetic breakdown between Fermi surfaces that are proximate to each other in reciprocal space. Theoretically, the oscillation frequencies of breakdown orbits can be decomposed into an algebraic combination of the primary F values (ref. 69). We find the four secondary frequencies are consistent with the algebraic combinations $F_3 - 2F_1$, $F_3 + F_1$, $F_4 + F_2$ and $F_5 + F_2$, respectively, supporting their origin in magnetic breakdown.

The T dependence of the dHvA oscillation amplitude A at fixed H can be used to extract the effective mass $m^\star$ of the band structure using the relationship

$$A(T,H) = A_0 \frac{2\pi^2 k_B T/\hbar\omega_c}{\sinh(2\pi^2 k_B T/\hbar\omega_c)} \quad (1)$$

where k_B is the Boltzmann constant, $\hbar$ is the reduced Planck constant and $\omega_c = e\mu_0 H/m^\star$ is the cyclotron frequency with e the elementary charge. In multi-band systems, interference between the numerous frequencies makes it difficult to isolate A for each band and extract their respective $m^\star$. We address this by disentangling individual F contributions using a band-pass filtering scheme in which the FFT of $\Delta M_\tau(1/H)$ at fixed T is multiplied by a boxcar function centred on the target F (see, for example, band-pass isolation of F_1; Extended Data Fig. 4b). We subsequently invert the filtered FFT that yields the disentangled contribution of F to $\Delta M_\tau(1/H)$ at fixed T. Extended Data Fig. 4c shows the contribution of F_1 to $\Delta M_\tau(1/H)$ at $\theta = 25.3°$ and various fixed T extracted using this procedure. Extended Data Fig. 4d shows the T dependence of the dHvA oscillation amplitude $A(T)$ extracted at fixed $1/(\mu_0 H)$ (distinct for each F contribution) along with fits to equation (1). We see a hierarchy of $m^\star$ paralleling their Fermi surface sizes ranging from $m^\star = 0.15m_0$ for F_1 to $m^\star = 1.02m_0$ for F_{10} (Extended Data Fig. 4d and Extended Data Table 2).

As discussed in the main text, quantum oscillations measured with H inclined at various fixed θ are aligned when plotted versus $H_\perp = H\cos\theta$, which is characteristic of a quasi-2D electronic structure (Fig. 2d). This is reinforced by examining the FFT spectra of these quantum oscillations (Extended Data Fig. 4e), which are qualitatively similar when plotted against $F\cos\theta$. The quasi-2D nature of the electronic structure is also apparent in the $H = 0$ transport properties. Examining Fig. 4a, we extract a normal state resistivity ratio between interlayer and intralayer transport, $\rho_c/\rho_\perp(T = 3\ \mathrm{K}) \approx 625$. We can use this to compare the interlayer (t_c) to intralayer (t_{ab}) hopping energy using the relation $\sqrt{\rho_c/\rho_\perp} \approx (t_{ab}/t_c)$ (ref. 70), where $t_c \approx 0.04t_{ab}$ is consistent with quasi-2D behaviour.

Extended Data Table 2 shows that compared with the relatively simple electronic structure of monolayer H-TaS_2 (Extended Data Fig. 4f,g, without and with SOC, respectively) in which the smallest pocket around K/K′ has $\mathcal{A} \approx 0.38\ \text{Å}^{-2}$, $SrTa_2S_5$ has a more complicated electronic structure with several small Fermi surfaces. This reflects the zone folding of the H-TaS_2 electronic structure into an order of magnitude smaller Brillouin zone. The large size of the unit cell makes including SOC in our calculations computationally challenging. Examining Fermi surface calculations for H-TaS_2 without and with SOC (Extended Data Figs. 4f,g, respectively), we see that SOC causes a splitting of Fermi surfaces. We find that $\mathcal{A}$ changes by about 10% in H-TaS_2 when SOC is included, consistent with the qualitative agreement we find between dHvA oscillations and computations for $SrTa_2S_5$ in Fig. 2b,c.

More broadly, the observation of quantum oscillations in $SrTa_2S_5$ is noteworthy, raising it as a platform to study unusual, quantum coherent phenomena anticipated in incommensurately modulated crystals[42]. High-mobility μ transport in incommensurately modulated H-TaS_2 layers of $SrTa_2S_5$ contrasts the relatively low mobilities observed in misfit TMD materials. For example, using a combination of optical reflectivity and plasmon resonance measurements, we estimate $\mu \approx 25\ \mathrm{cm^2\,V^{-1}s^{-1}}$ in H-TaS_2-based misfit TMDs[71], which is two orders of magnitude smaller than μ observed in $SrTa_2S_5$. Correspondingly, quantum oscillations have not been observed in the misfit TMDs. Although high μ transport has been observed in some incommensurately modulated organic metals (for example, $(MDT\text{-}TS)(AuI_2)_{0.441}$; ref. 34), the macroscopic uniformity of the structural modulation and robust, inorganic nature of $SrTa_2S_5$ raises it as a readily accessible platform to study phase-coherent electrons in incommensurately modulated metals.

Commensurability oscillations

Commensurability oscillations, first observed in semiconductor quantum wells[43,72], are $1/H$ periodic magnetoresistance oscillations that appear in 1D patterned 2D electron gases (2DEGs). Microscopically,

the oscillations arise from a $1/H$ periodic variation of Landau-level bandwidth by the 1D modulation

$$\Gamma_{CO} \propto J_0^2\left(\frac{2\pi r_c}{\lambda}\right) \approx \frac{1}{2}\left(1+\cos\left[2\pi\left(\frac{2r_c}{\lambda}-\frac{1}{4}\right)\right]\right) \quad (2)$$

where J_0 is a Bessel function of the first kind[44,73]. Examining equation (2), we see that their oscillation frequency is set by commensuration between the cyclotron diameter $2r_c = 2\hbar k_F/(e\mu_0 H)$ and the modulation λ—that is, $2r_c/\lambda = i$, where i is an integer. For patterned 2DEGs in which commensurability oscillations can be mapped at low H such that $2r_c/\lambda \gg 1$, semiclassical approximations can be used to describe their phenomenology. For example, the T suppression of commensurability oscillations at low H is captured by competition between the thermal smearing of the cyclotron radius δr_c and the modulation wavelength λ (ref. 74) (Extended Data Fig. 5a), which takes a Lifshitz–Kosevich (LK) form

$$A_{LK}(T) = A_0 \frac{T/T_{LK}}{\sinh(T/T_{LK})} \quad (3)$$

In $SrTa_2S_5$, however, we observe commensurability oscillations near the quantum limit of the underlying Fermi surface at which the semiclassical approximation breaks down. Using the band parameters deduced from quantum oscillations for the F_1 pocket that produces commensurability oscillations (main text and Extended Data Table 2), we estimate $E_F = \hbar^2 k_F^{\,2}/2m^\star \approx 3.7$ meV and $\hbar\omega_c \approx 7$ meV at $\mu_0 H^\star = 9.1$ T, in which commensurability oscillations appear (Fig. 3a). With $\hbar\omega_c > E_F$, this Fermi surface is near the quantum limit for $\mu_0 H > 9$ T. As Landau levels are well separated compared with E_F in this regime, r_c is no longer continuous and is instead quantized (Extended Data Fig. 5b) such that $r_c = \sqrt{2n+1}\,\ell_B$, where $\ell_B = \sqrt{\hbar/e\mu_0 H}$ is the magnetic length and n is the Landau-level index (note we recover the semiclassical expression $r_c = \hbar k_F/(e\mu_0 H)$ in the limit E_F much greater than $\hbar\omega_c$, where $n \approx E_F/\hbar\omega_c$). Correspondingly, we anticipate the thermal broadening of r_c will be a small contribution to the thermal suppression in the quantum limit (Extended Data Fig. 5b).

Instead of r_c smearing, T-dependent Landau-level broadening $\Gamma_T = \hbar/\tau_q(T)$ through a T-dependent quantum scattering rate $1/\tau_q(T)$ can suppress commensurability oscillations once $\Gamma_T \approx \Gamma_{CO}$ (equation (2)). The T dependence of $1/\tau_q$ is typically dictated by electron–electron scattering, $1/\tau_q(T) = 1/\tau_0 + 1/\tau_{ee}(T)$, where $1/\tau_0$ and $1/\tau_{ee}(T) = \eta T^2$ are the bare and electron–electron scattering rates, respectively. This affects commensurability oscillations through the Dingle suppression factor as[73,75]

$$A_D(T) \propto e^{-2\pi/\omega_c\tau_{ee}(T)} = A_0 e^{-\eta T^2} \quad (4)$$

Correspondingly, we fit the experimentally observed $A(T)$, the T-dependent commensurability oscillation amplitude at fixed $\mu_0 H^\star = 9.1$ T, with a thermal suppression function that combines equations (3) and (4),

$$A_{LK}(T) = A_0 e^{-\eta T^2} \frac{T/T_{LK}}{\sinh(T/T_{LK})} \quad (5)$$

Extended Data Fig. 5c shows the measured $A(T)$ (orange points) along with fits to equation (5) obtained by fixing T_{LK} and performing a least-squares fitting procedure to obtain the optimal A_0 and T_D, with satisfactory results for $T_{LK} \geq 30$ K in qualitative agreement with our estimates above.

Remarkably, the coherence of the structural modulation across macroscopic crystals permits observation of commensurability oscillations even in bulk transport measurements. Extended Data Fig. 5d,e shows magnetoresistance $MR_{\parallel}$ and $MR_{\perp}$, respectively, measured for the same bulk crystal with two different contact configurations (this crystal has well-defined satellite peaks, multi-domain structure as in Extended Data Fig. 2e obscures such effects). We see that there are oscillations persisting to high T in $MR_{\parallel}$ that are consistent with those seen in the FIB device (Fig. 3a). A weak contribution is also seen in the $MR_{\perp}$, which probably arises from mixing with $MR_{\parallel}$ due to contact misalignment. This effect is suppressed by the well-defined geometry of FIB patterned devices, allowing for a clear distinction between the behaviour of $MR_{\parallel}$ and $MR_{\perp}$ (Fig. 3a,b).

Properties of the superconducting state

Magnetization down to 0.39 K was measured with a SQUID magnetometer in a commercial magnetic property measurement system (Quantum Design MPMS3) equipped with a ^{3}He refrigerator. The temperature dependence of magnetic susceptibility $4\pi\chi(T)$ (CGS units) for a mosaic of several samples (c-axes aligned) was measured on warming with a constant external field $H_0 = 5$ Oe (parallel to the c-axes) after cooling to ^{3}He temperatures in zero field. We performed a demagnetization correction $H = H_0 - 4\pi NM$, where H is the effective field experienced by the sample, N is a demagnetization factor and M is the measured magnetization. Given the plate-like habit of the crystals, we use the asymptotic expression for high aspect ratio, prism-like samples[76]

$$N = 1 - \frac{2R}{\pi}\left[\ln\left(\frac{1}{R}\right) + 0.726\right] \quad (6)$$

where R is the thickness-to-length aspect ratio. We use $N = 0.9$ given $R \approx 0.06$ for these samples.

The separation of energy scales in $SrTa_2S_5$ between intralayer coherence at $T^\star = 2.5$ K and interlayer coherence at $T_c = 1.4$ K is striking. We performed additional transport characterization of intralayer transport to rule out extrinsic effects such as filamentary superconductivity (for example, $ZrTe_3$; refs. 77,78). Comparing the superconducting transitions measured with current I applied parallel and perpendicular to $\mathbf{q}$ for two different samples (Extended Data Fig. 6a), we find that resistivity drops to zero at the same T. We also measured V–J characteristics, where J is the current density, to extract the in-plane critical current J_{ab} density. Extended Data Fig. 6b shows V–J traces at various fixed T in the regime in which the intralayer resistivity is near zero, whereas the interlayer resistivity is finite, that is, $1.4\ \text{K} < T < 2.5$ K. The V–J traces become non-linear below $T = 2.4$ K, consistent with intralayer superconductivity below $T^\star$. Examining the V–J characteristics on a log–log plot, they appear to follow a power law $V \approx I^\alpha$, with α increasing monotonically with decreasing T (Extended Data Fig. 6c). These are signatures of a 2D Berezenskii–Kosterlitz–Thouless (BKT) transition[79] into the superconducting state; we estimate a BKT transition temperature $T_{BKT} \approx 1.9$ K, where the V–J curve most closely follows the anticipated $V \approx I^3$ dependence.

Qualitatively, by $T = 1.4$ K, the V–J curve is flat and featureless in the accessible J range (limited by sample heating) (Extended Data Fig. 6b), indicating that J_{ab} is beyond about 35 A cm^{-2}. Quantitatively, we extract a critical current density $J_{ab} \approx 18$ A cm^{-2} at $T = 1.75$ K (linear extrapolation of V–J at high J to zero V). This is of comparable order to $J_c \approx 10$ A cm^{-2} observed for interlayer transport (Fig. 4f). Given parasitic superconducting phases such as filamentary structures often exhibit small J_c (ref. 77), the sizeable intralayer and interlayer critical currents observed in $SrTa_2S_5$ suggests both transitions are intrinsic.

We also performed TDO measurements across the superconducting transition. In these measurements, an $SrTa_2S_5$ sample is placed within the inductive coil of an LC tank circuit, which is driven at its resonant frequency f by a tunnel diode-based bias circuit[80,81]. The inductive coil was constructed from 30 turns of 50 AWG (0.025 mm diameter) copper wire. The change in frequency was detected using a two-stage heterodyne setup to perform down-conversion of the TDO frequency into a more accessible range. Extended Data Fig. 6d

shows a schematic of the heterodyne circuit, wherein the $f \approx 120$ MHz signal from the TDO circuit is first mixed with a 170-MHz local oscillator, followed by a 50–60 MHZ local oscillator. As a result, the detected frequency f_O can be tuned into the range of approximately 1–5 MHz and isolated by a low-pass filter. The LC resonant f and detected f_O vary in tandem: if f increases (decreases) the measured f_O also increases (decreases).

For superconductors, variation of the coil inductance across the superconducting transition, and correspondingly f of the tank circuit, is tied to changes in their London penetration depth due to the onset of screening supercurrents[45,46]. Before loading an $SrTa_2S_5$ sample, we measured $f_O(T)$ of the tank circuit with an empty coil in the range $0.7\ \mathrm{K} < T < 3\ \mathrm{K}$ and found a monotonic decrease with decreasing T (Extended Data Fig. 6e). On repeating this measurement with an $SrTa_2S_5$ sample mounted with c-axis parallel to the axis n of the coil, we find a prominent f_O shift at $T^\star \approx 2.3$ K signalling the onset of in-plane supercurrents (Extended Data Fig. 6f), followed by a transition at lower $T \approx 1.4$ K. Measuring $f_O(T)$ with a sample mounted with ab-plane parallel to n reveals a transition at the lower T, indicating the onset of interlayer supercurrents (Extended Data Fig. 6g). As discussed in the main text, the feature at lower $T \approx 1.4$ K coincides with the Meissner transition in bulk susceptibility measurements. Qualitatively, the sizeable frequency shift $|\Delta f| \approx 300$ kHz in the range $1.4\ \mathrm{K} < T < T^\star$ is comparable to that observed in other bulk superconductors (similar sample and coil dimensions)[46], suggesting the onset of in-plane screening supercurrents is a bulk effect. Using the number of turns $N = 30$, total length $l = 0.75$ mm and bias current $I = 10$ mA applied to the coil during the TDO measurement, we can estimate the a.c. magnetic field $H_{\mathrm{a.c.}}$ applied to the sample during the measurement, $H_{\mathrm{a.c.}} = N \times I/l \approx 5$ Oe, which is small and comparable to H applied to measure $4\pi\chi(T)$ by SQUID.

We also find that superconductivity in $SrTa_2S_5$ is in the clean limit, established by comparing the in-plane Pippard coherence length $\xi_0 = 0.18\hbar v_F/k_B T_c$ with the normal state mean-free path $\ell = v_F\tau$, where v_F is the Fermi velocity, T_c is the superconducting transition temperature and τ is the normal state electron scattering time; in the clean limit $\xi_0/\ell = 0.18\hbar/(k_B T_c \tau) \ll 1$. As noted in the main text, the onset field of quantum oscillations $\mu_0 H_{\mathrm{onset}} \approx 3$ T yields a quantum mobility $\mu_q \approx 3{,}000\ \mathrm{cm^2\ V^{-1}\ s^{-1}}$. We can extract the quantum scattering time τ_q using the relation $\mu_q = e\tau_q/m^\star$. With $m^\star = 1.02m_0$ from the F_{10} oscillation, which is most likely to be the origin of superconductivity as the density of states in 2D systems is proportional to $m^\star$, we find $\tau_q = 1.7$ ps. We use $T_c = 2.5$ K where intralayer coherence is established, from which we obtain an upper limit $\xi_0/\ell \approx 0.3$, which positions $SrTa_2S_5$ in the clean limit of superconductivity.

Modulated superconductivity and suppressed interlayer coherence

Recent STM experiments[18–21] suggest spatially modulated parent states (for example, structural modulations or CDWs) can lead to PDW superconductivity. Using a Ginzburg–Landau model for coupled, coexisting orders[82,83], we can show that a PDW with the same periodicity as the modulated parent state can be favourable. We consider a Ginzburg–Landau free energy of the form

$$F = \int \mathrm{d}\mathbf{r}\left(f_\zeta^0(\mathbf{r}) + f_\Delta^0(\mathbf{r}) + \varepsilon\zeta^2|\Delta|^2\right) \tag{7}$$

where ζ and Δ are the order parameters for the parent modulation and superconducting state, respectively. The first two terms are the independent free energy densities of ζ and Δ orders whereas the last term is the usual biquadratic coupling between coexisting orders[82,83] with coupling constant ε.

Using equation (7), we can evaluate if modulated ζ of the form $\zeta(\mathbf{q}\cdot\mathbf{r}) = \zeta_0 + \zeta_1\sin(\mathbf{q}\cdot\mathbf{r})$, where ζ_0 is a uniform contribution and ζ_1 the modulation amplitude, favours modulated Δ. Together with the ansatz $\Delta(\mathbf{k}\cdot\mathbf{r}) = \Delta_0 + \Delta_1\sin(\mathbf{k}\cdot\mathbf{r} + \omega)$, where Δ_0 is the amplitude of uniform superconductivity, Δ_1 the PDW amplitude, $\mathbf{k}$ the PDW wavevector and ω is a phase shift, the biquadratic coupling term becomes

$$\varepsilon\zeta^2|\Delta|^2 \approx \varepsilon(\zeta_0^2|\Delta_0|^2 + \zeta_0\zeta_1(\Delta_0\Delta_1^\star + \mathrm{c.c.})\sin(\mathbf{q}\cdot\mathbf{r})\sin(\mathbf{k}\cdot\mathbf{r} + \omega)) \tag{8}$$

Note that Δ_0 and Δ_1 are complex-valued. Furthermore, terms proportional to $\sin(\mathbf{q}\cdot\mathbf{r})$ and $\sin(\mathbf{k}\cdot\mathbf{r} + \omega)$, which average to zero on integration over space have been dropped. For $\mathbf{k} = \mathbf{q}$, the second term in equation (8) becomes non-zero and couples the parent modulation ζ_1 to PDW order Δ_1. Averaging over one period $\lambda = 2\pi/|\mathbf{q}|$, we obtain

$$\varepsilon\zeta^2|\Delta|^2 \approx \varepsilon(\zeta_0^2|\Delta_0|^2 + \pi\zeta_0\zeta_1(\Delta_0\Delta_1^\star + \mathrm{c.c.})\cos(\omega)) \tag{9}$$

Examining equation (9), we see that the phase shift ω of the PDW relative to the parent modulation can be adjusted to make $\Delta_1 \neq 0$ energetically favourable (that is, the second term in equation (9) is negative).

Misorientation or misalignment of the PDW order between adjacent layers of a layered superconductor can suppress interlayer superconducting (that is, Josephson) coupling. A prominent example is the cuprate superconductor $La_{1.875}Ba_{0.125}CuO_4$ where 90° rotation of 1D PDW order between adjacent CuO_2 layers is thought to perfectly decouple them in the superconducting state. In fact, theory suggests coupling is non-zero for every fourth CuO_2 layer in the superconducting state[16], corresponding to an effective interlayer separation of about 24 Å. The inequivalent spatial modulation in adjacent H-TaS_2 layers of $SrTa_2S_5$ (Extended Data Fig. 2c) suggests that the modulated superconducting order is also inequivalent. Here we consider interlayer Josephson coupling C between layers with spatially modulated superconductivity that experiences a relative phase shift. Specifically, we consider a layer j with $\Delta^j = \Delta_0 + \Delta_1\sin(\mathbf{q}\cdot\mathbf{r})$ and an adjacent layer with $\Delta^{j+1} = \Delta_0 + \Delta_1\sin(\mathbf{q}\cdot\mathbf{r} + \kappa)$ (Extended Data Fig. 7a). The leading order coupling between these two layers is

$$C = \frac{c_0}{A}\int \mathrm{d}^2\mathbf{r}(\Delta^j(\Delta^{j+1})^\star + \mathrm{c.c.}) \tag{10}$$

where c_0 is a constant and A is the area of the sample. Evaluating equation (10), we obtain

$$C = c_0|\Delta_0|^2\left(1 + \frac{1}{2}\left|\frac{\Delta_1}{\Delta_0}\right|^2\cos(\kappa)\right) \tag{11}$$

Examining $\widetilde{C}(|\Delta_1/\Delta_0|, \kappa) = C(|\Delta_1/\Delta_0|, \kappa)/(c_0|\Delta_0|^2)$ (Extended Data Fig. 7b), the normalized Josephson coupling relative to the uniform superconducting state, we find C is suppressed relative to the uniform state for various configurations of $|\Delta_1/\Delta_0|$ and κ. In the regime $0 < |\Delta_1/\Delta_0| < \sqrt{2}$, we can find suppressed interlayer coupling (that is, $\widetilde{C} < 1$) for some values of κ. For $|\Delta_1/\Delta_0| = \sqrt{2}$, the interlayer coupling can be completely suppressed (that is, $\widetilde{C} = 0$) when the relative layer shift $\kappa = \pi$. In the pure PDW limit at which $|\Delta_1/\Delta_0| \gg 1$, the interlayer coupling is suppressed when $\kappa = \pi/2$. More broadly, this analysis suggests that interlayer coupling can generally be suppressed from phase-shifted, 1D modulated Δ.

Phase-sensitive test of PDW order by J_c anisotropy

It is predicted that interlayer critical current density J_c can provide global, phase-sensitive transport evidence of PDW order[12,13]. In general, J_c in a layered superconductor is given by

$$J_c = \mathrm{Im}\left[\frac{j_0}{A}\int \mathrm{d}^2\mathbf{r}(\Delta^j(\Delta^{j+1})^\star)\right] \tag{12}$$

where j labels the layer number. For $\Delta^j = \Delta_0 + \Delta_1 \sin(\mathbf{q}\cdot\mathbf{r})$ and $\Delta^{j+1} = \Delta_0 + \Delta_1 \sin(\mathbf{q}\cdot\mathbf{r} + \kappa)$, the oscillatory terms in equation (12) cancel, leaving behind a bare contribution to J_c from Δ_0. In the presence of an in-plane magnetic field $\mu_0 H_{ab}$ with corresponding vector potential $\mathbf{A}(\mathbf{r}) = \mu_0 H_{ab}(\sin(\varphi)x - \cos(\varphi)y)\hat{z}$, where φ is the in-plane angle of H_{ab} relative to $\hat{x}$, J_c gains a phase factor

$$J_c = \mathrm{Im}\left[\frac{j_0}{A}\int \mathrm{d}^2\mathbf{r}(\mathrm{e}^{2ie\mathbf{A}\cdot\hat{z}d/\hbar}\Delta^j(\Delta^{j+1})^\star)\right] \quad (13)$$

where d is the interlayer spacing. The new oscillatory phase factor due to $\mathbf{A}(\mathbf{r})$, equivalent to a Lorentz boost of the Cooper pairs, can interfere with the modulation in Δ and enhance J_c for particular φ. Setting $\mathbf{q}$ of the modulation parallel to $\hat{x}$ and expanding equation (13), we obtain

$$J_c(H_{ab},\varphi) = \mathrm{Im}\left[\frac{j_0}{A}\int \mathrm{d}^2\mathbf{r}(\mathrm{e}^{2ied(\mu_0 H_{ab}\sin(\varphi)x)/\hbar}\mathrm{e}^{-2ied(\mu_0 H_{ab}\cos(\varphi)y)/\hbar}\Delta^j(x)(\Delta^{j+1}(x))^\star)\right] \quad (14)$$

From equation (14), it is evident that J_c can be enhanced for $\varphi \approx \pi/2 + n\pi$ (H_{ab} perpendicular to $\mathbf{q}$), whereas the oscillatory terms average to zero for $\varphi \approx n\pi$ (H_{ab} parallel to $\mathbf{q}$), where n is an integer.

We performed a two-axis rotation measurement to map $J_c(H_{ab}, \varphi)$ for $SrTa_2S_5$. We first performed SAXS measurements to identify the orientation of the modulation $\mathbf{q}$ (Extended Data Fig. 8a,b). Extended Data Fig. 8c shows the two-axis rotator used for the measurement. The in-plane angle φ is controlled using a piezo rotator, whereas the angle θ is controlled by a string rotator. The θ–φ orientation of the samples was monitored using two orthogonal Hall sensors. Before loading into the cryostat, we measured the offset of the samples with respect to the Hall sensors that was used to determine the φ relative to $\mathbf{q}$ for each sample (Extended Data Fig. 8d). To minimize the c-axis component of magnetic field, for a given φ we scanned through θ at fixed $\mu_0 H$ while monitoring ρ_c (Extended Data Fig. 8e). As the upper critical field H_{c2} in layered superconductors is maximized for $H \perp c$, the θ that minimizes ρ_c also minimizes the c-axis component of H. This is done independently for each sample because they could have different alignments relative to the stage.

Extended Data Fig. 8f shows representative interlayer V–J characteristics at fixed $\mu_0 H_{ab} = 6$ T and $T = 0.3$ K for various φ. The critical current density J_c is defined as the J where V becomes non-zero. As shown in the main text, we find a prominent two-fold anisotropy in $J_c(H_{ab}, \varphi)$. We repeated this measurement for a second sample, sample B, and found similar anisotropy (Extended Data Fig. 8g) with J_c enhanced for $\varphi \approx \pi/2$; fitting to $J_c(H_{ab}, \varphi) = J_0(H_{ab}) + J_1(H_{ab})\cos^2(\varphi + \varphi_0)$, we find $\varphi_0 = 0.47\pi$. The two-fold anisotropy in $J_c(H_{ab}, \varphi)$ exhibited by both samples is consistent with predictions for mismatched 1D PDW order. Moreover, the relatively large in-plane anisotropy of $J_c(H_{ab}, \varphi)$, with $J_1/J_0 \approx 0.5$ at $\mu_0 H = 8$ T for both samples, suggests $|\Delta_1/\Delta_0|$ is sizeable, implying $SrTa_2S_5$ may be proximate to the regime in which $\widetilde{C}$ is completely suppressed (Extended Data Fig. 7b). It is noteworthy that for $\widetilde{C} \approx 0$, only every other H-TaS_2 layer separated by about 24 Å are coupled, which is similar to the j to $j+4$ layer separation in the cuprate $La_{1.875}Ba_{0.125}CuO_4$. In principle, this anisotropy could also arise from the anisotropic pinning of Josephson flux vortices formed between the superconducting layers for $H_{ab} \neq 0$. In terms of 1D PDW superconductivity, a stripe-modulated superconducting order parameter $\Delta(\mathbf{q}\cdot\mathbf{r})$ would make pinning anisotropic with respect to the stripes. More broadly, these results demonstrate strong coupling between the incommensurate structural stripe modulation and the superconducting state, and additionally highlight that incisive scattering and scanning probe measurements would be worthwhile to clarify the origins of the unconventional superconductivity in $SrTa_2S_5$.

Data availability

The data presented in the main text are available from the Harvard Dataverse[84]. All other data are available from the corresponding authors upon reasonable request.

Code availability

The codes used for the DFT and analytical calculations in this study are available from the corresponding authors upon reasonable request.

51. Meetsma, A., Wiegers, G. A., Haange, R. J. & de Boer, J. L. Structure of 2*H*-TaS_2. *Acta. Cryst. C* **46**, 1598–1599 (1990).
52. Tokura, Y. & Nagaosa, N. Nonreciprocal responses from non-centrosymmetric quantum materials. *Nat. Commun.* **9**, 3740 (2018).
53. Smidman, M., Salamon, M. B., Yuan, H. Q. & Agterberg, D. F. Superconductivity and spin–orbit coupling in non-centrosymmetric materials: a review. *Rep. Prog. Phys.* **80**, 036501 (2017).
54. Wochner, P., Tranquada, J. M., Buttrey, D. J. & Sachan, V. Neutron-diffraction study of stripe order in $La_2NiO_{4+\delta}$ with δ=2/15. *Phys. Rev. B* **57**, 1066–1078 (1998).
55. Hewat, E. A. et al. Superstructure of the superconductor $Bi_2Sr_2CaCu_2O_8$ by high-resolution electron microscopy. *Nature* **333**, 53–54 (1988).
56. Parsons, S. Introduction to twinning. *Acta Cryst. D* **59**, 1995–2003 (2003).
57. Zhang, Y., Yuan, N. F. Q. & Fu, L. Moiré quantum chemistry: charge transfer in transition metal dichalcogenide superlattices. *Phys. Rev. B* **102**, 201115 (2020).
58. Nam, N. N. T. & Koshino, M. Lattice relaxation and energy band modulation in twisted bilayer graphene. *Phys. Rev. B* **96**, 075311 (2017).
59. Turkel, S. et al. Orderly disorder in magic-angle twisted trilayer graphene. *Science* **376**, 193–199 (2022).
60. Wilson, J. A., Di Salvo, F. J. & Mahajan, S. Charge-density waves and superlattices in the metallic layered transition metal dichalcogenides. *Adv. Phys.* **24**, 117–201 (1975).
61. McMillan, W. L. Landau theory of charge-density waves in transition-metal dichalcogenides. *Phys. Rev. B* **12**, 1187–1196 (1975).
62. Kresse, G. & Furthmüller, J. Efficiency of ab-initio total energy calculations for metals and semiconductors using a plane-wave basis set. *Comput. Mater. Sci.* **6**, 15–50 (1996).
63. Kresse, G. & Furthmüller, J. Efficient iterative schemes for *ab initio* total-energy calculations using a plane-wave basis set. *Phys. Rev. B* **54**, 11169–11186 (1996).
64. Blöchl, P. E. Projector augmented-wave method. *Phys. Rev. B* **50**, 17953–17979 (1994).
65. Perdew, J. P., Burke, K. & Ernzerhof, M. Generalized gradient approximation made simple. *Phys. Rev. Lett.* **77**, 3865–3868 (1996).
66. Ku, W., Berlijn, T. & Lee, C.-C. Unfolding first-principles band structures. *Phys. Rev. Lett.* **104**, 216401 (2010).
67. Thomson, R. E., Burk, B., Zettl, A. & Clarke, J. Scanning tunneling microscopy of the charge-density-wave structure in 1*T*-TaS_2. *Phys. Rev. B* **49**, 16899–16916 (1994).
68. Onsager, L. Interpretation of the de Haas-van Alphen effect. *Lond. Edinb. Dubl. Philos. Mag. J. Sci.* **43**, 1006–1008 (1952).
69. Falicov, L. M. & Sievert, P. R. Magnetoresistance and magnetic breakdown. *Phys. Rev. Lett.* **12**, 558–561 (1964).
70. Lifshitz, E. M., Pitaevskii, L. P. & Landau, L. D. *Physical Kinetics*. (Pergamon, 1981).
71. Suzuki, K., Enoki, T. & Tajima, H. Optical reflectivity and carrier localization in incommensurate misfit layer compounds $(MS)_xTaS_2$ (*M*=rare-earth metal, Pb, Sn). *Phys. Rev. B* **52**, 16400–16409 (1995).
72. Peeters, F. M. & Vasilopoulos, P. Electrical and thermal properties of a two-dimensional electron gas in a one-dimensional periodic potential. *Phys. Rev. B* **46**, 4667–4680 (1992).
73. Raichev, O. E. Effect of Landau quantization on linear magnetoresistance of a periodically modulated two-dimensional electron gas. *Phys. Rev. B* **97**, 245310 (2018).
74. Beton, P. H. et al. Temperature dependence of magnetoresistance oscillations in a two-dimensional electron gas subjected to a periodic potential. *Phys. Rev. B* **42**, 9689–9692 (1990).
75. Bykov, A. A. et al. Modulation of magneto-intersubband oscillations in a one-dimensional lateral superlattice. *JETP Lett.* **110**, 354–358 (2019).
76. Joseph, R. I. Demagnetizing factors in nonellipsoidal samples—a review. *Geophysics* **41**, 1052–1054 (1976).
77. Nakajima, H., Nomura, K. & Sambongi, T. Anisotropic superconducting transition in $ZrTe_3$. *Physica B+C* **143**, 240–242 (1986).
78. Yamaya, K., Takayanagi, S. & Tanda, S. Mixed bulk-filament nature in superconductivity of the charge-density-wave conductor $ZrTe_3$. *Phys. Rev. B* **85**, 184513 (2012).
79. Halperin, B. I. & Nelson, D. R. Resistive transition in superconducting films. *J. Low Temp. Phys.* **36**, 599–616 (1979).
80. Van Degrift, C. T. Tunnel diode oscillator for 0.001 ppm measurements at low temperatures. *Rev. Sci. Instr.* **46**, 599–607 (1975).
81. Coffey, T. et al. Measuring radio frequency properties of materials in pulsed magnetic fields with a tunnel diode oscillator. *Rev. Sci. Instrum.* **71**, 4600–4606 (2000).
82. Weger, M. & Goldberg, I. B. in *Solid State Physics* Vol. 28 (eds Ehrenreich, H. et al.) 1–177 (Elsevier, 1974).
83. Imry, Y. On the statistical mechanics of coupled order parameters. *J. Phys. C Solid State Phys.* **8**, 567–577 (1975).
84. Devarakonda, A. et al. Replication data for: Evidence of striped electronic phases in a structurally-modulated superlattice. https://doi.org/10.7910/DVN/6KKJ6I (2024).
85. Monkhorst, H. J. & Pack, J. D. Special points for Brillouin-zone integrations. *Phys. Rev. B* **13**, 5188–5192 (1976).

Acknowledgements We thank E. Kaxiras, S. Y. F. Zhao, J. P. Wakefield and P. M. Neves for their discussions. This work was funded, in part, by the Gordon and Betty Moore Foundation EPiQS Initiative, grant no. GBMF9070 to J.G.C. (instrumentation development, DFT calculations), the US Department of Energy (DOE) Office of Science, Basic Energy Sciences, under award DE-SC0022028 (material development) and the Office of Naval Research (ONR) under award N00014-21-1-2591 (advanced characterization). A.D. acknowledges support from the Simons Foundation, Society of Fellows programme (grant no. 855186). D.C.B. acknowledges support from the STC Center for Integrated Quantum Materials (NSF grant DMR-1231319). A portion of this work was performed at the National High Magnetic Field Laboratory, which is supported by the National Science Foundation Cooperative Agreement (no. DMR-1644779), the State of Florida and the DOE. Use of the Advanced Photon Source at Argonne National Laboratory was supported by the DOE under contract no. DE-AC02-06CH11357.

Author contributions A.D. synthesized and characterized single crystals supported by T.S. and fabricated the FIB devices. A.D. and D.G. performed the electrical transport and torque magnetometry experiments. A.D., A.C. and D.G. performed the tunnel diode oscillator characterization. M.K. performed the SQUID magnetization experiments. A.J.K. and D.C.B. performed the electron microscopy experiments. A.D. performed the analytical calculations and S.F. performed the electronic structure calculations. A.D. and J.G.C. wrote the paper with contributions and discussions from all authors. J.G.C. supervised the project.

Competing interests The authors declare no competing interests.

Additional information

Correspondence and requests for materials should be addressed to J. G. Checkelsky.

Peer review information *Nature* thanks Philip Moll and the other, anonymous, reviewer(s) for their contribution to the peer review of this work.

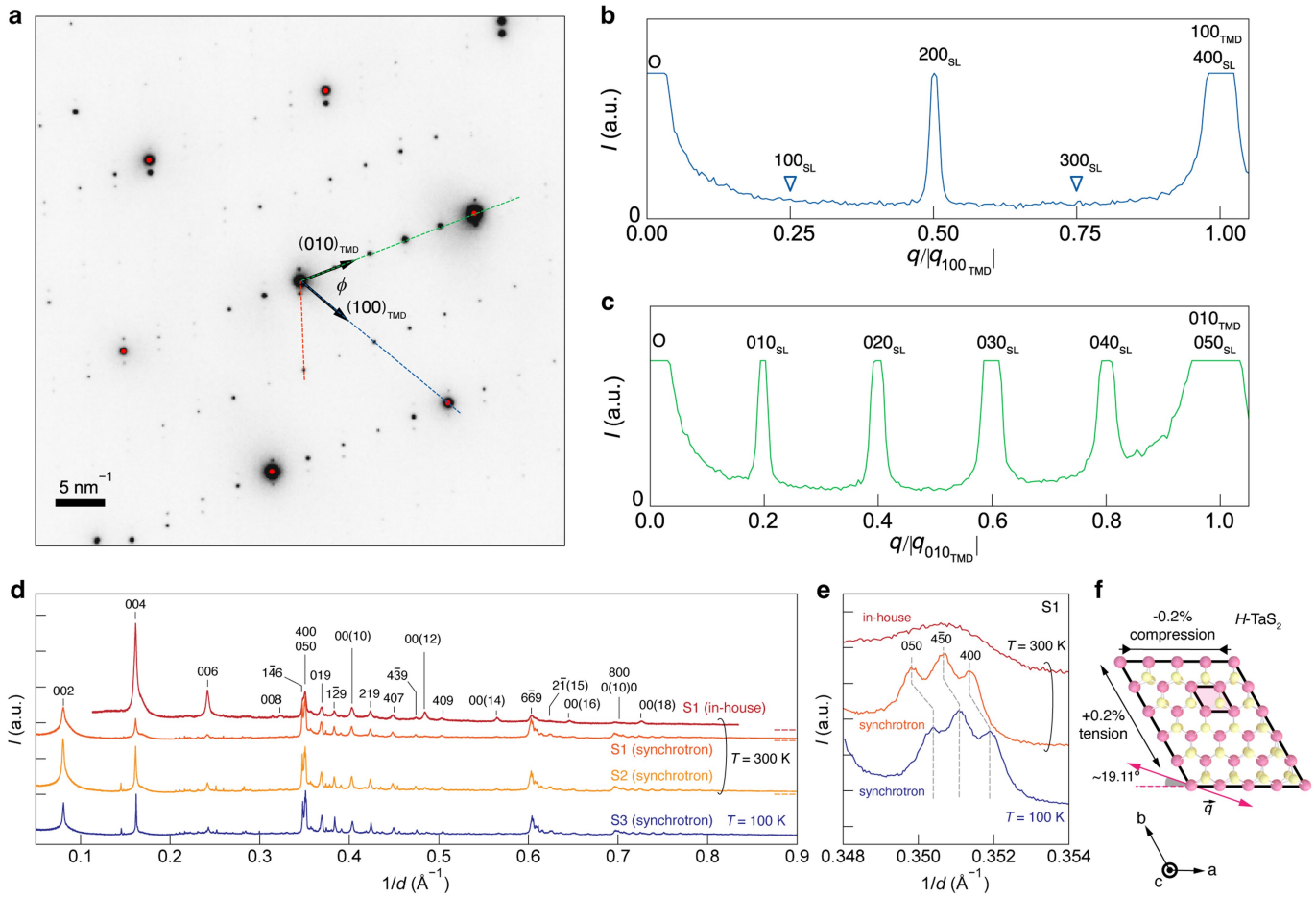

Extended Data Fig. 1 | Additional structural characterization of $SrTa_2S_5$. **a** Electron diffraction pattern from the in-plane structure. Red points mark peak positions of the strong reflections obtained by least-squares fitting to a 2D Gaussian profile. **b** Line-cut of the in-plane diffraction pattern along the (100) direction (dashed blue line in **a**). **c** Line-cut of the in-plane diffraction pattern along the (010) direction (dashed green line in **a**). Note the line-cut of the dashed red line in **a** is shown in Extended Data Fig. 2b. **d** In-house and synchrotron PXRD patterns indexed by the average model structure for $T = 300$ K and 100 K. **e** Zoom-in of the region around the (400) and (050) reflections which are split, indicative of in-plane strain. The pattern shift between 300 K and 100 K is consistent with thermal contraction of the unit cell. **f** Schematic of the in-plane strain imposed on the *H*-TaS_2 layer as determined from synchrotron PXRD. The modulation $\boldsymbol{q}$ is shown in magenta.

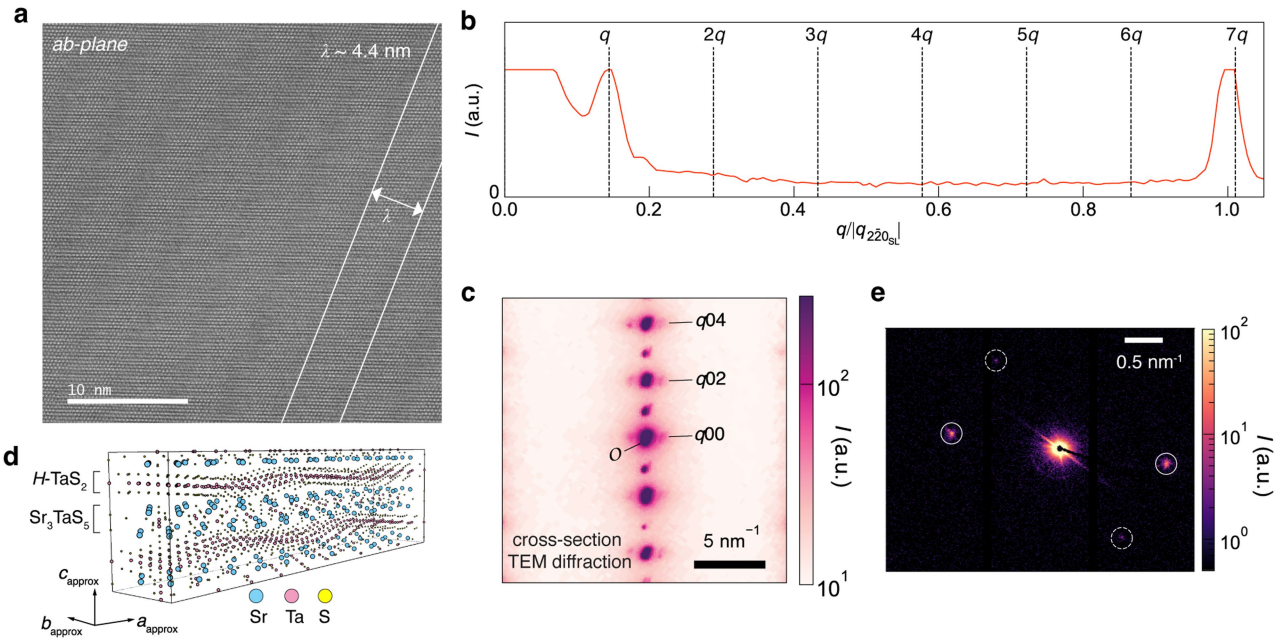

Extended Data Fig. 2 | Characterization of one-dimensional modulation. **a** Real-space TEM image of the *H*-TaS_2 layer where the periodic modulation can be seen. **b** Line-cut of electron diffraction pattern along the $(1\bar{1}0)_{SL}$ direction in reciprocal space (see dashed red line in Extended Data Fig. 1a) exhibiting incommensuration of **q** with the atomic lattice. **c** Electron diffraction pattern from the cross-section of $SrTa_2S_5$ shows the absence of ±**q** satellites peaks around the (00*n*) reflections for odd *n* due to an extinction condition. This is shown in *q*-vector units where real-space distances correspond to $d = 2\pi/|\mathbf{q}|$. **d** Perspective view of seven-fold approximant structure for the modulated structure. **e** SAXS experiments occasionally show weak ***q*** reflections oriented along multiple directions likely due to the fusing of multiple crystallites (also shown in *q*-vector units).

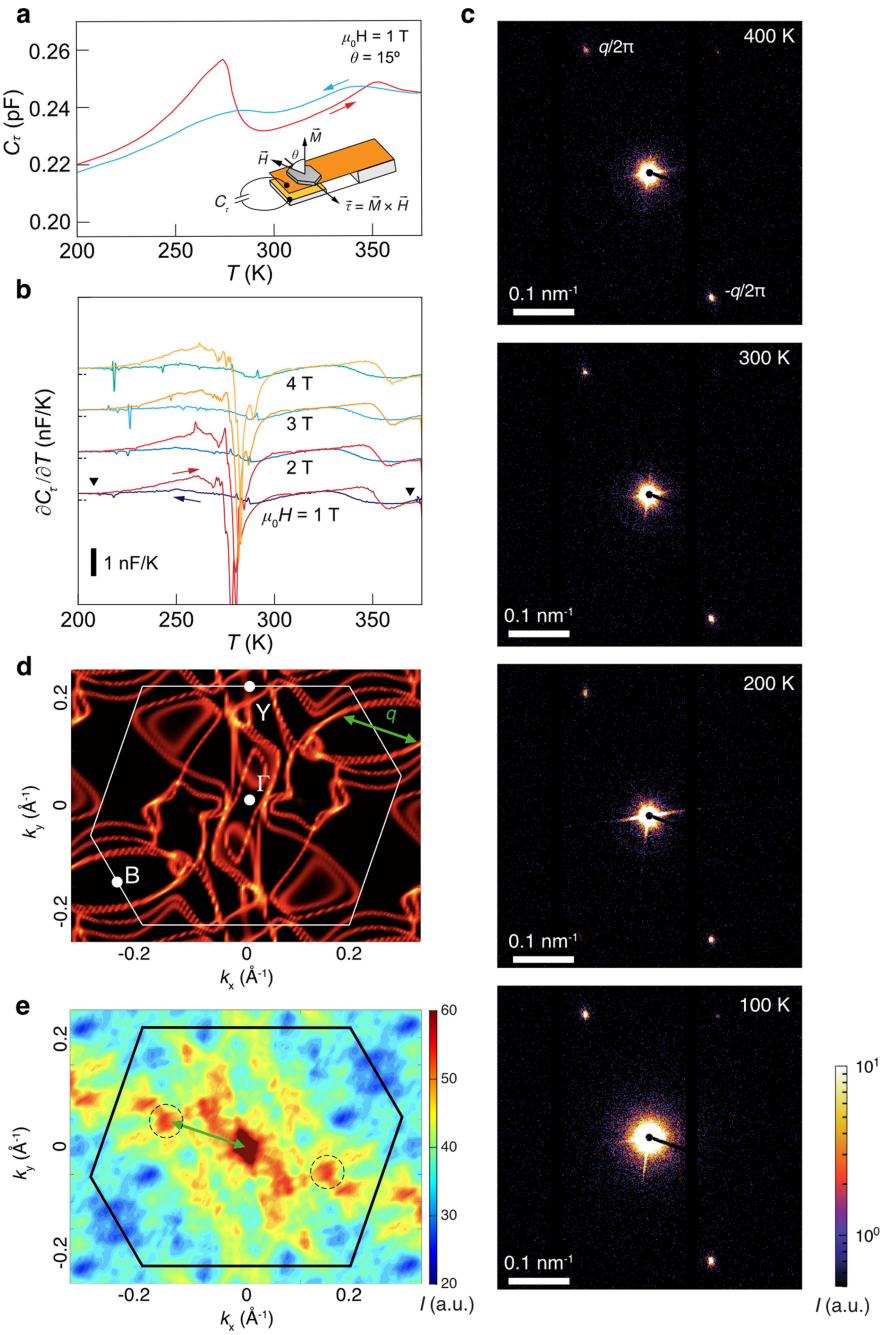

Extended Data Fig. 3 | Evidence of lock-in CDW. a Capacitively-detected magnetic torque response $C_\tau(T)$ of $SrTa_2S_5$ at fixed $\mu_0 H = 1$ T in the range 200 K < T < 375 K, measured on cooling (blue) and warming (red). **b** Temperature dependence of derivative $\partial C_\tau/\partial T$ measured on cooling and warming at various fixed H. **c** SAXS patterns collected at fixed T, cooling from 400 K to 100 K. **d** Contributions to the Fermiology of $SrTa_2S_5$ which originate from the K/K′ bands of H-TaS_2 (see Extended Data Fig. 4). **e** Auto-correlation map of the Fermiology in **d** showing a hotspot consistent with ***q***.

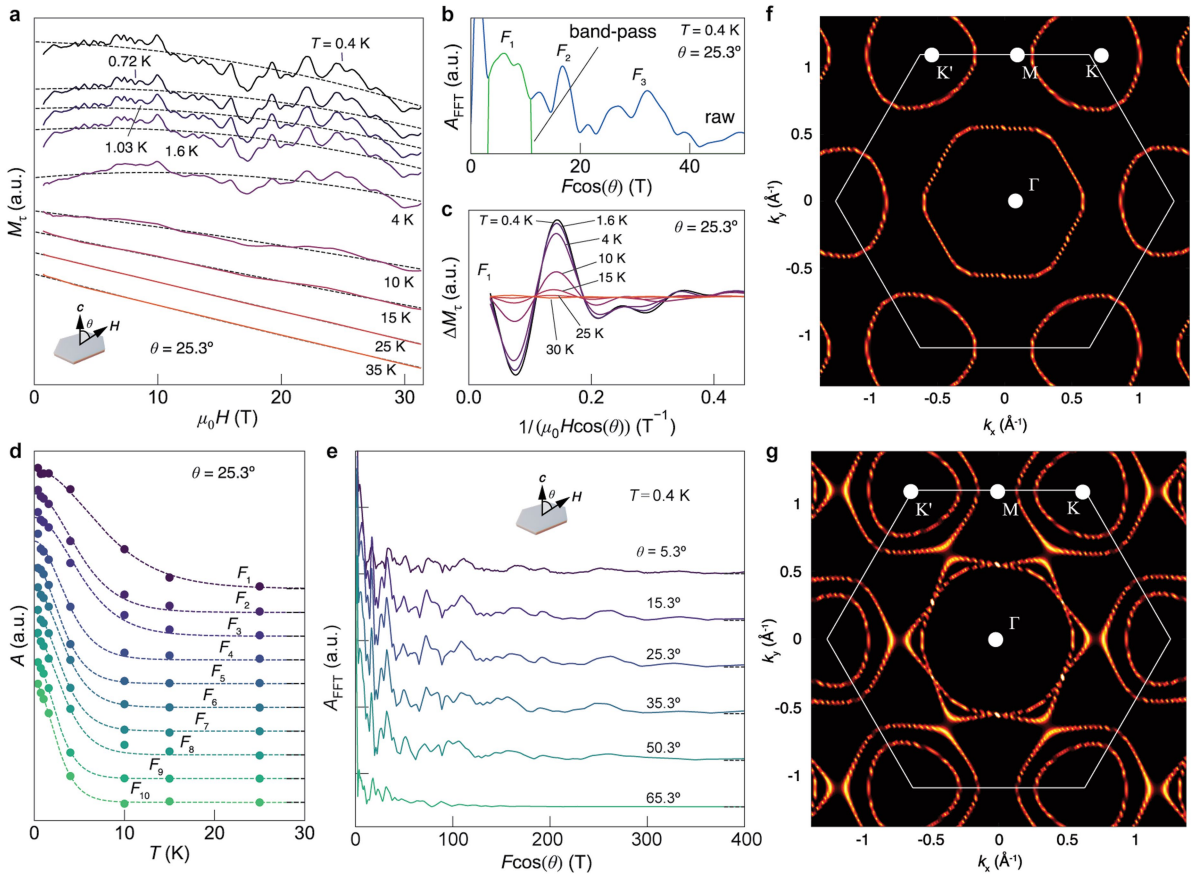

Extended Data Fig. 4 | de Haas-van Alphen quantum oscillations. a Torque magnetization M_τ at $\theta = 25.3°$ measured at various fixed T exhibits prominent quantum oscillations and dashed black lines are polynomial background fits (geometry shown in inset). Curves are vertically offset for clarity. **b** Raw FFT (blue) of background subtracted M_τ at $T = 0.4$ K and $\theta = 25.3°$ and the results of band-pass filtering to isolate the F_1 frequency component (green). **c** Isolated F_1 contribution to quantum oscillations at various fixed temperatures. **d** $A(T)$ for each frequency component with corresponding fits to equation (1) to extract their effective masses. Curves are vertically offset for clarity. **e** FFT spectra of quantum oscillations in torque magnetometry measured at $T = 0.4$ K with field oriented at various fixed angles θ relative to the c-axis (Fig. 2d). Calculated Fermi surfaces of monolayer H-TaS_2 **f** without and **g** with spin-orbit coupling. The Brillouin zone is shown with the white line. Calculations were performed using a $21 \times 21 \times 1$ Monkhorst-Pack grid sampling[85] with a 320 eV energy cutoff for the plane wave expansion.

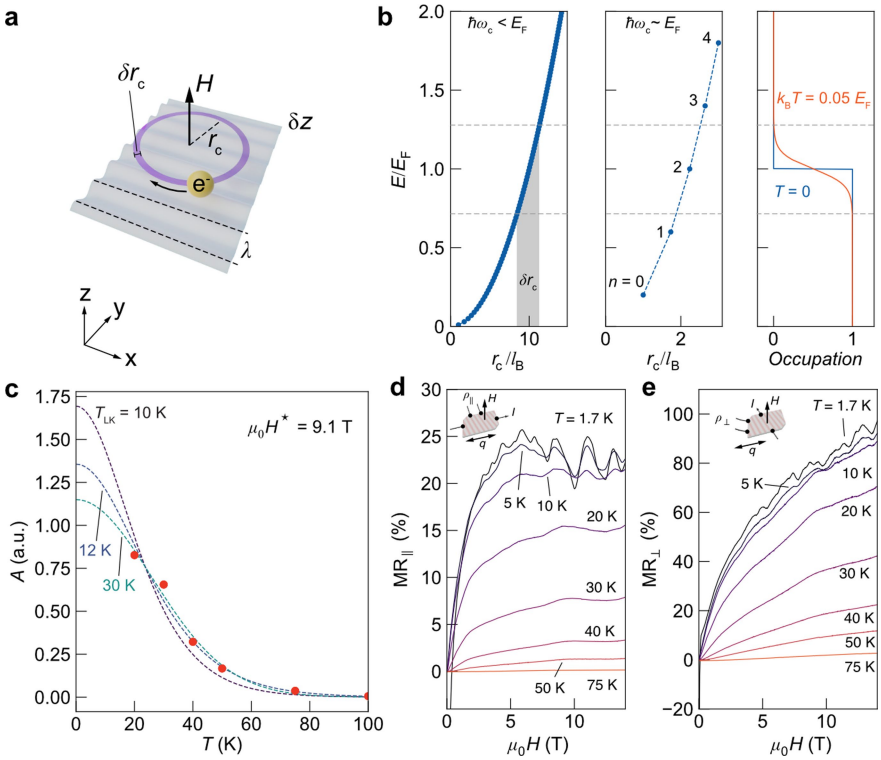

Extended Data Fig. 5 | Temperature dependence of commensurability oscillations and additional measurements. a Commensurability oscillations arise from commensuration between the cyclotron diameter $2r_c$ and the 1D modulation wavelength λ. In the semiclassical limit, thermal broadening of the cyclotron radius δr_c beyond λ suppresses the oscillations. **b** In the semiclassical regime with $\hbar\omega_c < E_F$ (left), thermal broadening of the Fermi-Dirac (FD) distribution (right) leads to finite δr_c. Near the quantum limit $\hbar\omega_c \sim E_F$ (middle), however, thermal broadening of the FD distribution must become comparable to $\hbar\omega_c$ for δr_c to become non-zero. **c** $A(T)$ at $\mu_0 H^\star = 9.1$ T (red points) with a least-squares fits for various fixed T_{LK} to a form containing both Lifshitz-Kosevich and Dingle factors (equation (5)). $A(T)$ is extracted by subtracting a monotonic background from $MR_{\parallel}$ (Fig. 3a). **d** $MR_{\parallel}(H)$ and **e** $MR_{\perp}(H)$ at various T measured for the same bulk crystal with two different contact configurations (see inset).

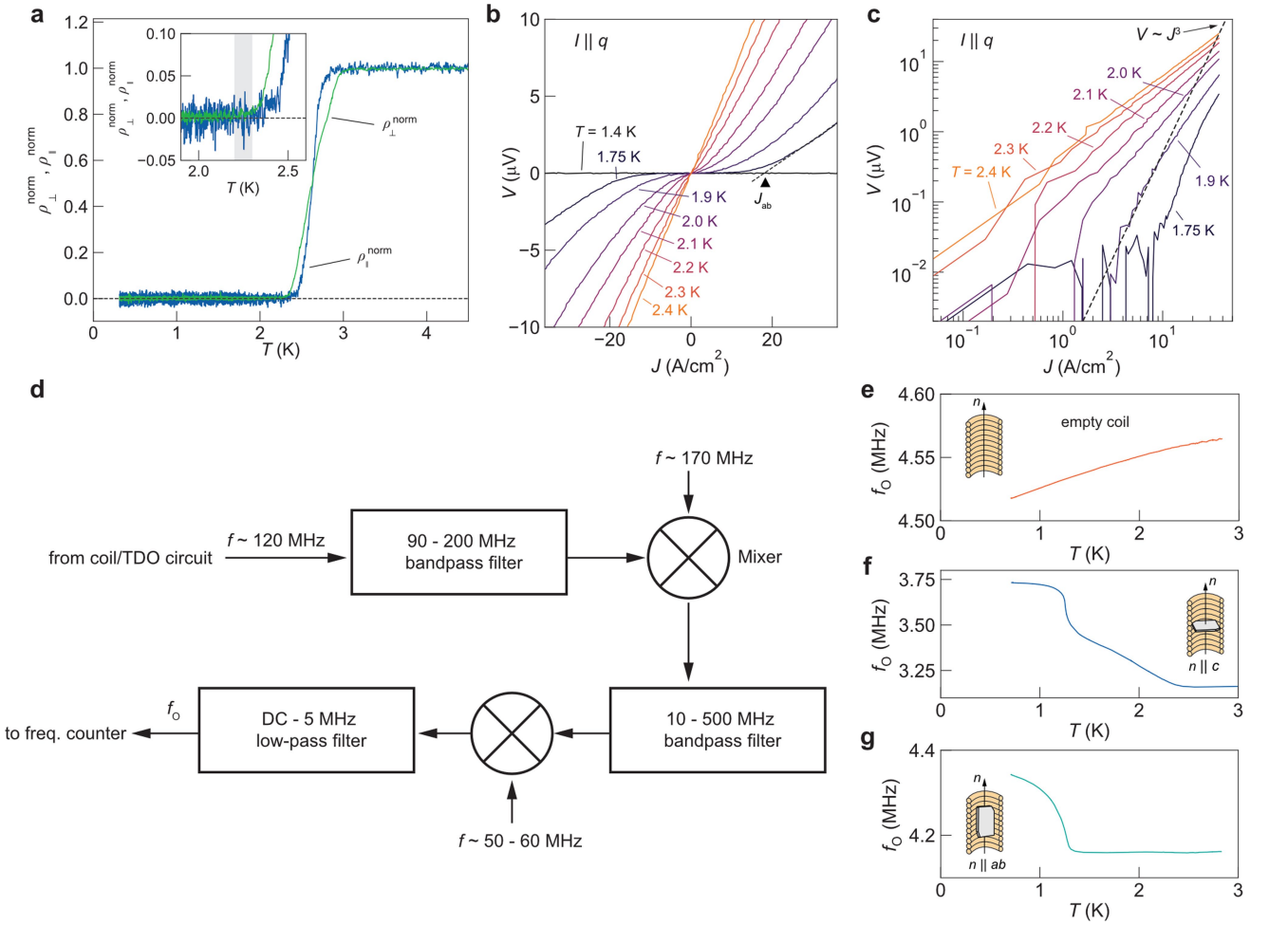

Extended Data Fig. 6 | Superconducting transition in transport and tunnel diode measurements. a Intralayer resistivities measured parallel and perpendicular to **q** normalized to their values at $T = 4$ K, $\rho_{\parallel}^{\mathrm{norm}}(T)$ and $\rho_{\perp}^{\mathrm{norm}}(T)$, respectively. (inset) Both quantities reach zero at $T \approx 2.3$ K, in agreement with other measures of the intralayer coherence temperature. **b** Intralayer *V*–*J* characteristics (**I** || **q**) measured at various fixed *T*. The critical current density J_{ab} is extracted by extrapolation from the high *J* linear regime to zero *V*. **c** *V*–*J* characteristics from **b** in the range $1.7\ \mathrm{K} < T < 2.5\ \mathrm{K}$ plotted on a log-log scale to extract the BKT transition temperature. **d** Schematic two-stage heterodyne circuit used to extract LC coil resonant frequency. *T*-dependent output frequency from heterodyne circuit $f_O(T)$ of the TDO circuit with **e** an empty coil **f** $SrTa_2S_5$ sample mounted within the coil with *c*-axis parallel to coil axis *n*, and **g** $SrTa_2S_5$ sample mounted with *ab*-plane parallel to *n*.

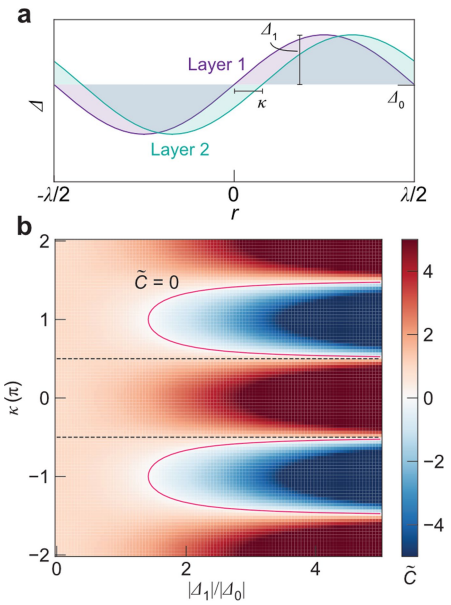

Extended Data Fig. 7 | Phase-shifted superconducting order and interlayer coupling. a We consider interlayer coupling between superconducting layers hosting 1D modulated $\Delta(\mathbf{k}\cdot\mathbf{r})$. We allow for a relative phase shift κ of $\Delta(\mathbf{k}\cdot\mathbf{r})$ between the layers. **b** Normalized interlayer coupling $\widetilde{C}$ as a function of $|\Delta_1/\Delta_0|$ and κ. The magenta line traces where $\widetilde{C}=0$.

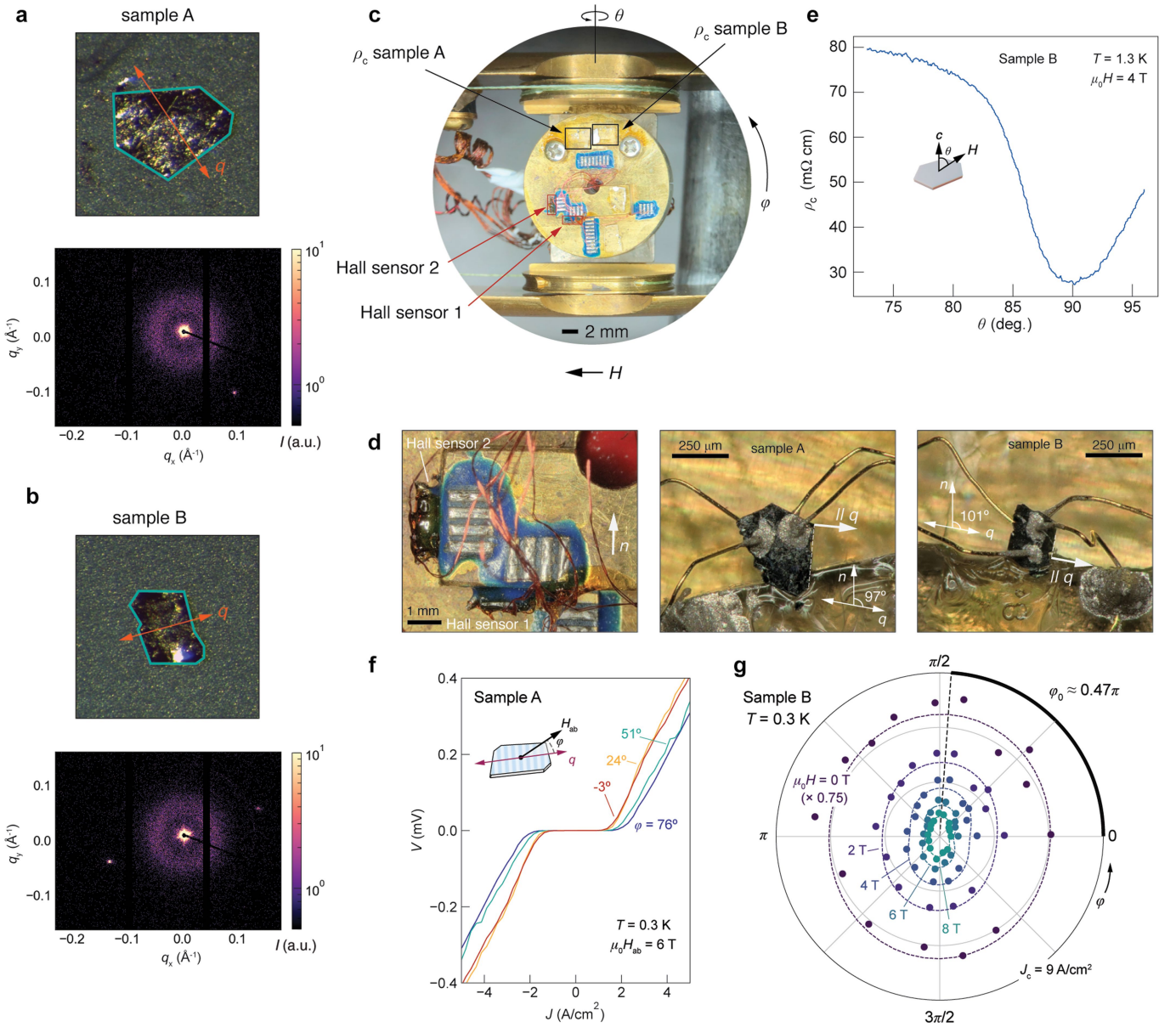

Extended Data Fig. 8 | Measuring in-plane field dependence of interlayer critical current. a (top) Optical image of sample A with its modulation **q** shown in orange (bottom) SAXS pattern used to determine the orientation of **q**. **b** (top) Optical image of sample B with **q** orientation shown in orange. (bottom) Corresponding SAXS pattern used to determine the orientation of **q**. **c** Image of two-axis rotator setup. Samples A and B are mounted on a piezorotator, which provides φ rotation. This piezo sits on a larger cradle which allows for θ rotation. Two Hall sensors are used to determine the θ-φ orientation. **d** Close-up optical images of the (left) Hall sensors, (middle) sample A, and (right) sample B. The angle offset between the sample **q**'s and Hall sensor was used to determine φ relative to H_{ab}. **e** For a given φ, we performed a θ scan while measuring ρ_c at fixed **H** to align **H** to the *ab*-plane. **f** Representative interlayer *V*–*J* characteristics (sample A) at $\mu_0 H_{ab}$ = 6 T and T = 0.3 K for various fixed φ. **g** Polar plot of interlayer critical current density J_c for sample B versus in-plane magnetic field orientation $H_{ab}(\varphi)$ exhibiting prominent two-fold anisotropy.

Extended Data Table 1 | Average model structure for $SrTa_2S_5$ in atomic coordinates

Space group No. 14, $P112_1/a$ (c-axis unique)
a = 13.17 Å, b = 16.47 Å, c = 24.81 Å, γ = 120°

Atom	*x*	*y*	*z*	Atom	*x*	*y*	*z*
Sr	0	3/5	0.5835	Sr	1/4	2/5	0.5835
Sr	1/2	4/5	0.5835	Sr	1/4	4/5	0.4165
Sr	1/2	3/5	0.4165	Sr	3/4	0	0.4165
Ta	0	0	1/4	Ta	1/4	1/5	1/4
Ta	0	1/5	1/4	Ta	1/4	2/5	1/4
Ta	0	2/5	1/4	Ta	1/4	3/5	1/4
Ta	0	3/5	1/4	Ta	1/4	1/5	1/2
Ta	0	4/5	1/4	Ta	3/4	2/5	1/2
Ta	1/4	0	1/4	Ta	3/4	4/5	1/4
S	1/12	2/15	0.3128	S	1/3	2/15	0.3128
S	7/15	2/15	0.3128	S	5/6	2/15	0.3128
S	1/12	1/3	0.3128	S	1/3	1/3	0.3128
S	7/12	1/3	0.3128	S	5/6	1/3	0.3128
S	1/12	8/15	0.3128	S	1/3	8/15	0.3128
S	7/12	8/15	0.3128	S	5/6	8/15	0.3128
S	1/12	11/15	0.3128	S	1/3	11/15	0.3128
S	7/12	11/15	0.3128	S	5/6	11/15	0.3128
S	1/12	14/15	0.3128	S	1/3	14/15	0.3128
S	7/12	14/15	0.3128	S	5/6	14/15	0.3128
S	1/4	3/5	0.59189	S	1/4	0.46945	0.46932
S	0.08681	3/5	0.46932	S	0.41319	0.73055	0.46932
S	1/4	0.06945	0.46932	S	0.41319	0.33055	0.46932
S	0.08681	1/5	0.46932	S	1/4	1/5	0.59189
S	1/2	1	0.5536	S	0	0	0.4464

All constituent atoms occupy the Wyckoff position 4e with site symmetry 1.

Extended Data Table 2 | Band parameters from quantum oscillations

	F (T)	$\mathcal{A}$ (Å^{-2})	k_F (Å^{-1})	m^* (m_0)
F_1	4.4	4.2×10^{-4}	0.012	0.15
F_2	16.4	1.6×10^{-3}	0.023	0.21
F_3	34.9	3.3×10^{-3}	0.032	0.22
F_4	51.7	4.9×10^{-3}	0.039	0.30
F_5	76.0	7.3×10^{-3}	0.048	0.42
F_6	112.0	1.1×10^{-2}	0.059	0.55
F_7	170.0	1.6×10^{-2}	0.071	0.63
F_8	195.7	1.9×10^{-2}	0.078	0.61
F_9	257.3	2.5×10^{-2}	0.089	0.92
F_{10}	335.9	3.2×10^{-2}	0.101	1.02

Oscillation frequencies F, Fermi surface cross-section $\mathcal{A}$, Fermi wavevector k_F, and effective mass m^* from dHvA measurements. Note k_F is obtained by assuming circular Fermi surfaces.